RIVULET FLOW AND STABILITY

by

MARGARET HONGXIA LIANG

BASc.(Engineering Physics) University of British Columbia, 2000

A THESIS SUBMITTED IN PARTIAL FULFILLMENT OF

THE REQUIREMENTS FOR THE DEGREE OF

MASTER OF SCIENCE

in

THE FACULTY OF GRADUATE STUDIES

Department of Mathematics
Institute of Applied Mathematics

We accept this thesis as conforming
to the required standard

.....

.....

.....

.....

.....

THE UNIVERSITY OF BRITISH COLUMBIA

December 2002

(Signature) _____

Department of Mathematics
The University of British Columbia
Vancouver, Canada

Date _____

Abstract

Two dimensional, steady-state rivulet flow down an inclined plane, and combined rivulet/air flow in a circular pipe are studied. Both asymptotic analysis and numerical methods are used to solve the Navier-Stoke equations for rivulet flow down an inclined plane. Asymptotic approximation, which is valid only for rivulet of large cross-sectional aspect ratios, is substantiated by exact numerical solutions up to specified error tolerance. Standard shooting techniques are used to solve ODE for rivulet shape and finite element methods are used to approximate the flow velocity. The stability of the rivulet flow is also studied based on energy criterion. We find that pure gravity driven rivulets are subject to break up and pure shear driven rivulets are stable in that sense. For the combined air/rivulet flow, the relationship between pressure gradients and fluxes is investigated using the annulus rivulet and circular arc rivulet models. The annulus rivulet model is solved analytically, and the circular arc rivulet is computed using FEMLAB. It is found that pressure gradient needed to drive the rivulet flow is much more sensitive to change in channel size than to change in contact angle. Finally, linear stability analysis of the combined air/rivulet flow in a rectangular domain is formulated.

Table of Contents

List of Tables

List of Figures

Acknowledgement

I am grateful for the supervision and support of Dr. Brian Wetton. I would also like to thank Tim Myers, who develeped the asymptotoics of small aspect ratio for rivulets described in the beginning of chapter two. This work is partly funded by MITACS. I also like to thank all the friends, colleagues and faculty members who have helped me so much along the way.

Chapter 1
Introduction

1.1 Background

When liquid flows down an inclined flat surface, several different flow regimes can be observed. The flow regimes depend mostly on the flow rate, the physical properties of the liquid-solid surface system and the inclination of the surface. The flow pattern could be droplets, linear rivulets, meanders, pendulum rivulets, or even in sheets [3]. We will investigate water flow in the linear rivulet region in this thesis.

A rivulet is a stream of liquid flowing on a solid surface under a gas with (basically) unidirectional flow perpendicular to the rivulet cross section. The mathematical interest begins with the study of the motion of a thin continuous film driven by body or surface forces over a dry substrate. At some stage, the continuous film will break up at the leading edge into a series of distinct rivulets or droplets. Modeling this behavior requires the examination of distinct regions, namely, the thin continuous film, the moving contact line and the rivulet[2]. Thin film flow, with one free surface, is already relatively well understood by applying lubrication theory[1]. However, as the width of a film decreases into the rivulet region, thin film approximation becomes invalid. In this thesis, we will study the steady flow of a single rivulet, driven by inter-facial shear and gravity. The physical quantities that are usually considered are: gravitational forces, incompressble viscous fluid mechanics (often in a thin film approximation), surface tension of the liquid gas interface, and the contact angle at the solid-liquid-gas interface. There is no "front" to the rivulet and therefore no need to address the issue of moving contact line.

Rivulet flow plays an important role in a number of industrial processes, including gas-liquid contacting equipment in distillation and absorption, dry patch formation on heated surfaces, liquid film drainage from steam turbine stator blades, etc. Specifically, in heat exchanges, interfacial shear, caused by the over lying gas flow, plays a significant role. Here, the break-up of a film into rivulets may have disastrous consequences[2]. The aerospace industry also has an interest in rivulet flow driven by air shear, when considering the de-icing of air-plane wings. The problem occurs because ice formation or snow accumulation on airplane wings poses a threat to safety of flight. During a period after take-off and before the liquid is finally blown off, it forms rivulets and flows as "run-back" water which affect the aerodynamic behavior of the wings. Knowledge of this flow and consequently how far back the aerofoil requires heating is essential in developing an anti-icing strategy.

The most recent industrial interest to the understanding of a rivulet flow arises from modelling the proton exchange membrane fuel cell (PEMFC), which is also the initial motivation of this thesis. The connections between fuel cells and rivulet flow are described in details below. In all of the above areas, a knowledge of the fluid motion and stability characteristics of rivulet flow is required to assess the efficiency of the process.

1.2 Application to fuel cells

A fuel cell basically converts electro-chemical into electrical energy with high efficiency, and in some cases, with zero pollution. There are many different types of fuel cells, such as the proton exchange membrane hydrogen fuel cell, alkaline fuel cell, molten carbonate fuel cell, and direct methanol fuel cell etc. Although different types of fuel cells all have their unique characteristics, they are all environment friendly power generators. Fuel cell technology existed since 1839, but only recently have fuel cells gained popular recognition and come under serious consideration as an economically and technically viable power source. Due to increased concerns of pollution caused by automobiles and power plants, several companies have put a lot of effort into the development of fuel cells. For example, some car manufacturers are hoping to commercially produce fuel cell powered cars in 2004.

PEMFCs require hydrogen and oxygen as inputs, oxygen is often supplied by ambient air. The reaction is catalyzed by a thin layer of Platinum, to which the reactant gases are delivered via a series of pressurized flow fields on either side of Nafion membrane. The membrane is permeable to only small positive ions, like the H+ ions, and is supported by a gas diffusion electrode(GDE) which is currently commonly made from a porous teflonated carbon fibre paper. The GDE allows reactant gases to reach the active catalyst sites on the fuel cell membrane and carries current away from the sites. Figure (1.1) below illustrates the structure of a PEMFC on the cathode side. On top of the Platinum coating, there is the anode GDE and then the

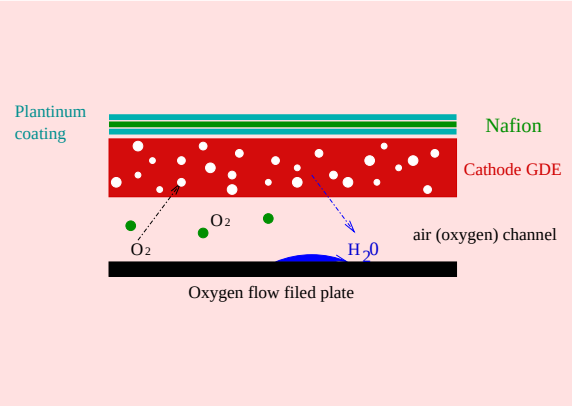

Figure 1.1: Cross section of a PEMFC.

hydrogen channel.

During the reaction process, water is formed on the cathode side and accumulates in the oxygen channel. Though water is important to maintain the humidity level of the channel so the membrane remain well hydrated, excess amount of liquid water in the gas flow channels can reduce the efficiency of the fuel cell significantly by blocking the channel, and so inhibiting the diffusion of gas through the medium, thereby prevents reaction from occurring. Thus "water management" inside the fuel cell is very important to achieve high efficiency. Since the excess amount of water in channels is carried out using the gas shear flow, it places an extra load on the compressor used to pump reactant gasses throught the fuel cell. This is an important design consideration.

1.3 Mathematical formulation

Consider a Newtonian rivulet flow down a channel with cross section boundary Γ. shown in Fiugre 1.2. The surface of the rivulet $h(x)$ divides the domain into region 1 and region 2.

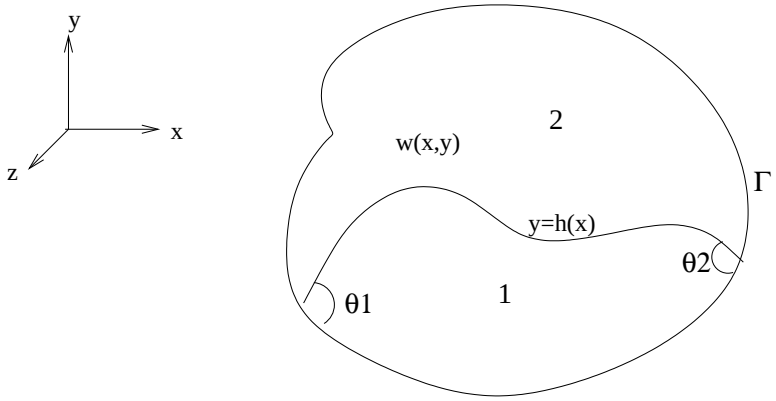

Figure 1.2: Cross-section of a rivulet on a flat surface. The flow velocity $w(x, y)$ is perpendicular to the page.

The dynamics of a viscous incompressible fluid are governed by the Navier-Stokes equation [6].

$$\rho \frac{\partial \vec{u}}{\partial t} + (\vec{u} \cdot \nabla)\vec{u} = f - \nabla p + \mu \nabla^2 \vec{u} \tag{1.1}$$

together with the continuity equation $\nabla \cdot \vec{u} = 0$. The terms are:

- ρ: density of fluid
- $\vec{u}$: velocity of fluid
- μ: viscosity of fluid
- f: external force (including gravity)
- p: pressure gradient

The rivulet flow is modeled under the following assumptions:

1. the fluid is incompressible,

2. the flow has reached a steady-state,

3. the flow is fully developed, that is, it is unidirectional and the derivatives in the direction of flow are negligible.

Assumptions 2 and 3 indicate the velocity field is specified by $\vec{u} = (0, 0, w(x, y))$, and we also assume that gravity is the only external force, so the Navier-Stokes equation reduces to

$$-\nabla p + \mu \nabla^2 \vec{u} + \rho \vec{G} = 0 \tag{1.2}$$

where $\vec{G} = (G_1, G_2, G_3) = \rho g(0, g \cdot \hat{y}, g \cdot \hat{z})$ after decomposing the gravitational force into y and z directions ($\hat{z}$ denotes the unit vector in z direction). Component wise, we have:

$$-\frac{\partial p}{\partial x} = 0 \tag{1.3}$$

$$-\frac{\partial p}{\partial y} + G_2 = 0 \tag{1.4}$$

$$-\frac{\partial p}{\partial z} + \mu \Delta w + G_3 = 0 \tag{1.5}$$

Note that the continuity equation is automatically satisfied.

Equations (1.3) and (1.4) can be solved to obtain:

$$p = G_2 y + C_0(z) + C_1. \tag{1.6}$$

This can be substituted into equation (1.5), resulting in:

$$-C_0'(z) + \mu \Delta w + G_3 = 0. \tag{1.7}$$

Since w is independent of z, and C_0 is a function of z only, both terms have to equal to a constant in order for the equation to hold. Let $-C_0'(z) = \lambda$, then

$$\lambda + \mu \Delta w + G_3 = 0 \tag{1.8}$$

Also,

$$p = -\lambda z + G_2 y + C \tag{1.9}$$

Appropriate boundary and interface conditions for the system are:

(a) No-slip at the fluid-solid boundary Γ,

$$w(x, y) = 0, \tag{1.10}$$

(b) Continuity of velocity at free surface $y = h(x)$,

$$[w] = w_1 - w_2 = 0 \tag{1.11}$$

(c) Continuity of shear stress at free surface,

$$\mu[w_n] = \mu(w_{n1} - w_{n2}) = 0 \tag{1.12}$$

(d) Balance of normal stress at interface,

$$[p] = p_2 - p_1 = \sigma\kappa \tag{1.13}$$

where κ is the curvature of the surface. If it contacts boundary with contact angle $\theta_1 = \theta_2$, then

$$\kappa = \frac{h_{xx}}{(1 + h_x^2)^{3/2}}$$

We will consider special cases of rivulet flow in the later chapters. In chapters 2 and 3, we will study rivulet flow down an inclined plane, using both numerical and asymptotic techniques. The analytical solution requires the rivulet aspect ratio to be small. The numerical investigation is carried out without these restrictions. This allows us to verify the analytical solutions and also ascertain their region of validity. In chapter 4, we assume rivulet flow down a flat circular channel, and investigate the relationship between fluxes and pressure gradient needed to drive the flow, which is of particular interest to fuel cell design. MATLAB and FEMLAB [11] are used to solve the problems numerically. Finally, the important question of whether a rivulet will break-up into two or more sub-rivulets is addressed. A limited stability study based on energy criterion is done in chapter 3, and a more rigorous linear stability analysis is shown in chapter 6.

Chapter 2

Rivulet Flow Down an Inclined Plane – Asymptotic Analysis

Consider a rivulet of width L and height $y = h(x)$ flowing down an inclined surface inclined at angle α to the horizontal as shown in figure (2.1) below.

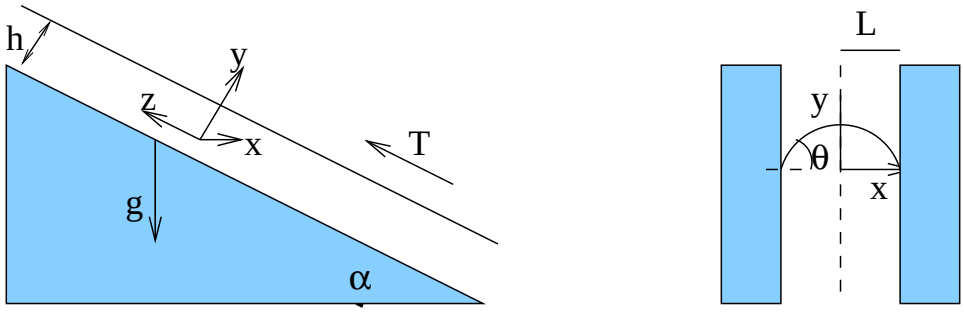

Figure 2.1: Cross-section of a rivulet on a flat surface.

In this case, the problem is simplified in the following sense.

1. It is assumed that air provides the tangential stress T only, so boundary condition (1.11) is not applied. Condition (1.12) becomes $\mu w_n = T$.

2. Air pressure is constant, so $p = p_a + \sigma\kappa$ for all z. Thus equation (1.9) becomes

$$p = G_2 y + C = G_2 h(x) + C = p_a + \sigma\kappa \tag{2.1}$$

Differentiate the equation above, to obtain the Laplace-Young equation,

$$G_2 \frac{\partial h}{\partial x} = -\sigma \frac{\partial}{\partial x}\left(\frac{h_{xx}}{(1+h_x^2)^{3/2}}\right) \tag{2.2}$$

with $G_2 = \rho g \cos(\alpha)$.

Besides the previous assumptions, we also assume the aspect ratio $\epsilon = H/L$ (where H is the height scale) is small, so that terms of $O(\epsilon^2)$ are negligible, and do an asymptotic analysis of the problem.

First, we non-dimensionalize the components of the Navier-Stokes equations, and they are:

$$p_x = 0 \,, \tag{2.3}$$

$$w_{yy} - B + \epsilon^2 w_{xx} = 0 \,, \tag{2.4}$$

$$p_y = -1 \,. \tag{2.5}$$

Where $B = \rho g H^2 \sin\alpha/(\mu W)$ is the Bond number, represents the ratio of gravitational to viscous forces. All variables are related to the dimensional quantities (denoted by hats) by

$$\hat{p} \to \rho g H \cos\alpha \; p \qquad \hat{w} \to W w$$
$$\hat{x} \to L x \qquad \hat{y} \to H y \qquad \hat{T} = \frac{\mu W}{H} T$$

The choice of velocity scale, W, depends on whether gravity or surface shear is the primary driving force. If gravity dominates the flow then $W = \rho g H^2 \sin\alpha/\mu$ and the Bond number $B = 1$. If air shear drives the flow then $W = (H\hat{T}/\mu)$. To keep the most general model, the velocity scale will be left unspecified in the following analysis.

Appropriate boundary conditions become:

$$w(x,0) = 0 \qquad \frac{\partial w}{\partial y} - \epsilon^2 \left(\frac{\partial h}{\partial x}\frac{\partial w}{\partial x} + \frac{1}{2}\frac{\partial w}{\partial y}\left(\frac{\partial h}{\partial x}\right)^2 \right) = T \Big|_{y=h} \qquad \frac{\partial w}{\partial x} = 0 \Big|_{x=0} \tag{2.6}$$

$$p = -C^{-1} h_{xx} \left[1 - \epsilon^2 h_x^2 + \cdots \right] \,. \tag{2.7}$$

These represent no-slip at the solid surface, continuity of shear stress at the free surface, symmetry about the center-line and continuity of normal stress at the free surface respectively. The non-dimensional number $C^{-1} = \sigma/(\rho g L^2 \cos\alpha)$ is the inverse capillary number, where C resp-resents the ratio of viscous to gravitational forces. Note, we assumed $\epsilon h_x \ll 1$ in the pressure expansion which requires a relatively small liquid/solid contact angle.

The form of the system (2.3)-(2.7) indicates there exists a series solution in powers of ϵ^2 for h, w and p. Integration of (2.5), subject to (2.7), immediately, gives the series for pressure in terms of the unknown functions h_i:

$$p = (h_0 - y) - C^{-1}h_{0_{xx}} + \epsilon^2 \left[h_1 + C^{-1}\left(h_{0_{xx}}h_{0_x}^2 - h_{1_{xx}}\right)\right] + \cdots \ . \tag{2.8}$$

The terms in the film height series are determined by substituting for pressure in (2.3),

$$h_{0_{xxx}} - Ch_{0_x} = 0 \ , \tag{2.9}$$

$$h_{1_{xxx}} - Ch_{1_x} = \frac{\partial}{\partial x}\left[h_{0_x}^2 h_{0_{xx}}\right] \ . \tag{2.10}$$

The appropriate boundary conditions are,

$$h_{i_x}(0) = 0 \ , \qquad h_i(1) = 0 \tag{2.11}$$

and either

$$\int_0^1 h_0 dx = \frac{A}{2LH} \ , \qquad \int_0^1 h_i dx = 0 \tag{2.12}$$

or

$$h_{0_x}(1) = -\frac{L\tan\theta}{H} \ , \qquad h_{i_x}(1) = 0 \ . \tag{2.13}$$

Conditions (2.11) state there is symmetry about the mid-point, at the edge the height is zero. Condition (2.12) relies on the cross-sectional area, A, being a measurable quantity, while (2.13) uses the contact angle. Solve for h_i and get:

$$h_0 = \kappa(\cosh(\sqrt{C}x) - \cosh(\sqrt{C})) \ , \tag{2.14}$$

$$h_1 = a_1(\cosh(\sqrt{C}x) - \cosh(\sqrt{C})) + f(x) - f(1) \ , \tag{2.15}$$

where

$$f(x) = -\frac{\kappa^3 C\sinh(\sqrt{C}x)}{8}(\sqrt{C}x - \sinh(\sqrt{C}x)\cosh(\sqrt{C}x)) \ , \tag{2.16}$$

$$a_1 = -\frac{f_x(1)}{\sqrt{C}\sinh(\sqrt{C})} \ , \tag{2.17}$$

$$\tag{2.18}$$

and $\kappa = -L\tan\theta/H\sqrt{C}\sinh(\sqrt{C})$. The height-scale H is chosen such that $h_0(0) = 1$, in which case,

$$H = \frac{L\tan\theta(\cosh(\sqrt{C})-1)}{\sqrt{C}\sinh(\sqrt{C})} \ , \ \kappa = -\frac{1}{\cosh(\sqrt{C})-1} \ . \tag{2.19}$$

The fluid velocity is found by integrating (2.4), subject to (2.6) and apply on $y = h_0+\epsilon^2 h_1+\cdots$,

$$w(x,y) = b_0 y + B\frac{y^2}{2} + \epsilon^2\left(b_1 y + Bh_{0_{xx}}\frac{y^3}{6}\right) + \cdots \ , \tag{2.20}$$

where

$$b_0 = T - Bh_0 \ , \tag{2.21}$$

$$b_1 = -Bh_1 - \frac{Bh_{0_{xx}}h_0^2}{2} - Bh_0 h_{0_x}^2 + \frac{Th_{0_{xx}}^2}{2} \ . \tag{2.22}$$

To highlight the effect of the driving forces on the fluid flux and permit a relatively simple analytical solution, only the leading order terms will be considered from now on. The fluid flux down the slope, $Q_0 = \hat{Q}_0/(LHW)$, is defined as

$$Q_0 = -\int w_0(x,y)dA_0 = -2\int_0^1\int_0^{h_0(x)} w_0(x,y)dydx \tag{2.23}$$

$$= 2\int_0^1 B\frac{h_0^3}{3} - T\frac{h_0^2}{2}dx \ . \tag{2.24}$$

This integrates to

$$Q_0 = \frac{2}{3}B\kappa^3\left[\frac{2s}{3\sqrt{C}} + \frac{11sc^2}{6\sqrt{C}} - \frac{3c}{2} - c^3\right] - T\kappa^2\left[c^2 - \frac{3cs}{2\sqrt{C}} + \frac{1}{2}\right] \ , \tag{2.25}$$

where $s = \sinh\sqrt{C}$ and $c = \cosh\sqrt{C}$. Limiting values for small C (narrow rivulets, low density or high surface tension) and large C can now be calculated.

For small C,

$$Q_0 = -2\kappa^2\left(\frac{2}{105}\kappa BC^3 + \frac{T}{15}C^2\right) \tag{2.26}$$

for large C

$$Q_0 = -\frac{\kappa^2 e^{2\sqrt{C}}}{24}\left(2\kappa Be^{\sqrt{C}} + 3T\right) \ . \tag{2.27}$$

The role of inter facial shear on flux can be clearly seen from the preceding equations. For example, in the small C limit (and note that $\kappa < 0$) a positive air shear, $T > 0$, acts against

gravity and so decreases the flux down the slope. When $T = -2\kappa BC/7$ the air shear exactly balances gravity and the net flux is zero. A value of T below this will result in a fluid flux down the slope.

In dimensional form, the limiting expressions (2.26), (2.27) for flux become

$$\hat{Q} = \frac{4}{105}\frac{\rho g \sin\alpha}{\mu} L^4 \tan^3\theta - \frac{2\hat{T}}{15\mu} L^3 \tan^2\theta \tag{2.28}$$

$$\hat{Q} = \frac{2}{3}\frac{\rho g \sin\alpha}{C^{3/2}\mu} L^4 \tan^3\theta - \frac{\hat{T}}{2\mu C} L^3 \tan^2\theta \ , \tag{2.29}$$

respectively.

It is interesting to note that the small C solution, equation (2.28), associated with high surface tension, in fact does not involve surface tension. Another point of interest is that the above results depend either upon $\tan^3\theta$ or $\tan^2\theta$, indicating that accurate measurement of the contact angle is crucial, particularly for values of θ much less or much greater than $45°$.

As $L \to \infty$, the height-scale H is identified as the approximately constant central height (the limiting value of (2.19a)), giving $H = \tan\theta\sqrt{\sigma/(\rho g \cos\alpha)}$ and $C = L^2 \tan^2\theta / H^2$. Substituting this into (2.29) leads to an expression for the dimensional flux/unit width:

$$\frac{\hat{Q}_0}{2L} \to \frac{\rho g H^3 \sin\alpha}{3\mu} - \frac{\hat{T}H^2}{2\mu} \ , \tag{2.30}$$

which is the result obtained from the two dimensional analysis for a fluid sheet given in Myers & Thompson [5].

The energy/unit length of a rivulet involves kinetic, potential and surface energies and also viscous dissipation. The sum of these must remain constant, although the individual terms may alter. Under the current model assumptions and provided the flow is isothermal, it is clear that as the rivulet moves down the slope its kinetic and surface energies remain constant since w and h are independent of z. Potential energy will be lost and this must be balanced by viscous dissipation. The sum of kinetic and surface energies per unit length is,

$$E = \frac{\hat{E}}{\rho L H V^2} = \frac{1}{2}\int_{-1}^{1}\int_{0}^{h} v^2 \, dydx + \frac{P\sigma + 2(\sigma_{sl} - \sigma_{sg})}{\rho H V^2} \ , \tag{2.31}$$

where A is the cross-sectional area, σ_{sl} and σ_{sg} are the surface/liquid and surface/gas interfacial tensions, P is the perimeter of the liquid-gas interface.

Taking the leading order velocity terms from equation (2.20) and setting $h = h_0$ the kinetic energy per unit length, K, is asymptotically

$$K = \int_0^1 \int_0^{h_0} \left(b_0 y + B\frac{y^2}{2} \right)^2 dy dx \tag{2.32}$$

$$= \int_0^1 \frac{b_0^2}{3} h_0^3 + \frac{B b_0}{4} h_0^4 + \frac{B^2}{20} h_0^5 dx \ . \tag{2.33}$$

Substituting for $h_0(x)$ and integrating leads to

$$K = \left(a_0 + a_1 T + a_2 T^2 \right) \ , \tag{2.34}$$

where

$$\begin{aligned} a_0 &= -\frac{B^2\kappa^5}{900} \cdot \frac{-64s - 607c^2 s + 120c^5\sqrt{C} - 274c^4 s + 600c^3\sqrt{C} + 225c\sqrt{C}}{\sqrt{C}} \\ a_1 &= -\frac{5B\kappa^4}{288} \cdot \frac{72c^2\sqrt{C} + 9\sqrt{C} - 50sc^3 + 24c^4\sqrt{C} - 55cs}{\sqrt{C}} \ , \\ a_2 &= -\frac{\kappa^3}{18} \cdot \frac{6c^3 mL - 4\,s + 9c\sqrt{C} - 11c^2 s}{\sqrt{C}} \ . \end{aligned}$$

The perimeter length, to leading order, is the same as the rivulet width

$$P = 2\int_0^1 \sqrt{1 + \epsilon^2 h_x^2}\, dx = 2 + \mathcal{O}(\epsilon^2) \ . \tag{2.35}$$

The Young-Duprés equation[12]provides a relation between the surface tensions:

$$\sigma_{sl} - \sigma_{sg} = -\sigma\cos\theta \ . \tag{2.36}$$

Although, as is frequently pointed out, this implies a unique contact angle which may only be achieved on extremely smooth surfaces, hence it does not account for hysteresis. The leading order analytic expression for the energy E is therefore

$$E = K + \frac{2\sigma}{\rho H V^2}\left(1 - \cos\theta\right) \ , \tag{2.37}$$

where K is specified by equation (2.34).

It is at this stage that the advantage of the current method over lubrication theory becomes apparent; the kinetic energy term enters the energy balance at leading order. It would only do so in the lubrication approximation provided certain other restrictions are satisfied. To apply lubrication theory the reduced Reynolds number $\delta^2 R_e = \delta^2 \rho V L/\mu \ll 1$. The kinetic energy $\sim \rho H L V^2 \ll \mu^2/(\delta^3 \rho)$ (in order to satisfy $\delta^2 R_e \ll 1$). The surface energy $\sim \sigma L$. Taking typical values for a water rivulet of dimensions $L \times H$ =1cm x 1mm shows the kinetic energy must then be significantly less than 10^{-6}. The surface energy is $\mathcal{O}(10^{-3})$. The kinetic energy would therefore not enter the leading order energy balance in this case. In fact, for water flow the energy calculation will only be valid under lubrication theory when $\delta^2 H \ll 10^{-8}$m.

For both shear driven($\alpha = 0$) and gravity driven($T = 0$) large L flow, the asymptotic fluxes can be derived from equations (2.28) and (2.29), and the asymptotic energy behaviour can be derived from equation (2.37) and we find $Q \propto L$, and $E \propto L$, so we conclude:

$$E \propto Q$$

for both shear and gravity driven, large L flow. The results also make sense physically. For L large, the rivulet will be like a flat sheet for most of the region (see Figure 3.2 for rivulet shape when $L = 5cm$). So E and Q both vary linearly with length L.

The leading order asymptotic behaviour is different for small L. The equations derived above won't apply in this case since they are only valid for ϵ small which corresponds to large L. We can get the asymptotic results for small L as follows. For L small, the cross section of a rivulet looks like a semi-circle. The dominate energy is the surface energy which proportional to arclength which is πL in this case. So we have

$$E \propto L$$

which is valid for both shear and gravity driven flow.

For fluxes we need to consider the two cases separately. First nondimensionalize the general equation $\mu \Delta w = \lambda$. Let $x \to L\hat{x}$, $y \to L\hat{y}$, where $\hat{x}$ and $\hat{y}$ are nondimensional quantities. Thus

$$\Delta w = \frac{\partial^2 w}{\partial x^2} + \frac{\partial^2 w}{\partial y^2} = \frac{1}{L^2}\left(\frac{\partial^2 w}{\partial \hat{x}^2} + \frac{\partial^2 w}{\partial \hat{y}^2}\right)$$

For gravity driven flow, we are solving $\Delta w = G$ in the domain with Dirichelet boundary conditions, where $G \propto area = \pi L^2$. To get flux, we need to integrate w over the domain, the area of the cross section. It results another factor of L^2. Thus we get

$$Q \propto L^4$$

for this case.

For shear driven flow, we solve $\Delta w = 0$ in the domain and $\partial w/\partial n = TL$ on the circular arc and Dirichelet condition on the bottom. So we have

$$Q \propto L^3$$

In summary, we should expect

$$E \propto Q^{1/4}$$

for gravity driven small L flow, and

$$E \propto Q^{1/3}$$

for shear driven small L flow. These results are reflected in the numerical solutions in chapter 3, the asymptotics are also needed to fill in the gaps in the numerical results.

Chapter 3
Rivulet Flow On An Inclined Plane – Numerical Method

3.1 Numerical method

Consider a rivulet flows down an inclined plane shown in Figure 2.1. To solve the problem numerically, we compute the cross section of the rivulet first by applying the Laplace-Young equation (2.2).

$$\rho g \cos(\alpha) h_x = -\sigma \frac{d}{dx}\left(\frac{h_{xx}}{(1+h_x^2)^{3/2}}\right) \tag{3.1}$$

which governs the height h(x)of the rivulet.

Integrate the equation with respect to x, we obtain:

$$\frac{h_{xx}}{(1+h_x^2)^{3/2}} = \frac{\rho g \cos(\alpha)}{\sigma} h + C \tag{3.2}$$

where C is a constant that is to be determined along with the profile h(x) for given symmetric half length L $[h(\pm L) = 0]$ and surface contact angle θ $[\tan\theta = h_x(\pm L)]$. Note that the left hand side of (3.2) is the curvature of the rivulet.

Equation (3.2) is a second order differential equation. To reduce it to first order, we parametrize the equation in arclength s. Let $x = x(s)$ and $y = h = y(s)$. Then,

$$|(x^{''}, y^{''})| - \frac{\rho g \cos(\alpha)}{\sigma} y = C \tag{3.3}$$

Also,

$$|(x^{'}, y^{'})| = 1 \tag{3.4}$$

Differentiate (3.4) get:

$$x^{'}x^{''} + y^{'}y^{''} = 0 \tag{3.5}$$

$$(x^{''})^2 + (y^{''})^2 = (C + \frac{\rho g \cos(\alpha)}{\sigma} y)^2 \tag{3.6}$$

Introduce a new variable ϕ, the angle of the tangent line on the surface of the rivulet, shown in Figure 3.1.

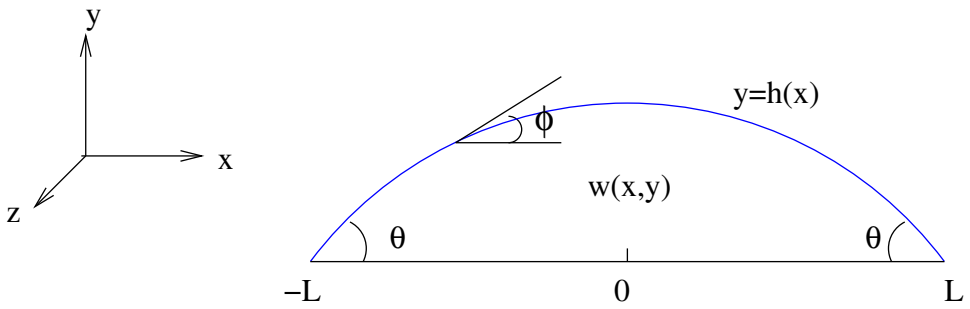

Figure 3.1: Cross-section of a rivulet on a flat surface.

Then $x^{'} = \cos(\phi)$ and $y^{'} = \sin(\phi)$. The curvature κ satisfies:

$$\kappa^2 = (x^{''})^2 + (y^{''})^2 \tag{3.7}$$

$$= (-\sin(\phi)\phi^{'})^2 + (\cos(\phi)\phi^{'})^2 \tag{3.8}$$

$$= (\phi^{'})^2 \tag{3.9}$$

Thus equation (3.2) becomes:

$$\begin{pmatrix} x \\ y \\ \phi \end{pmatrix}^{'} = \begin{pmatrix} \cos(\phi) \\ \sin(\phi) \\ C + \frac{\rho g \cos\alpha}{\sigma} y \end{pmatrix} \tag{3.10}$$

with the initial conditions(s=0):

$$\begin{pmatrix} x(0) \\ y(0) \\ \phi(0) \end{pmatrix} = \begin{pmatrix} -L \\ 0 \\ \theta \end{pmatrix} \tag{3.11}$$

This arc-length parametrized formulation not only simplifies the equation to first order, but also enables us to compute rivulet shapes with contact angles greater than 90^o without additional

work, although this capability is not used in this study where we are aiming at comparing to asymptotics suited for small angles.

Cross section

The ODE solver capability in MATLAB is used to compute the cross section geometry. We used a shooting method to determine C such that $\phi(s^*) = 0$ where s^* satisfies $x(s^*) = 0$, a symmetry condition that would imply the original condition at x=L.

Figure 3.2 below shows the rivulet cross-section obtained from both the analytical formula, equation(2.19) and the numerical method described above, for water flowing down a plane with $\alpha = \theta = 15^o$. L takes the values of $5mm$ and $5cm$. No results are shown for $L < 5mm$ since these are virtually identical to the $5mm$ graph, similarly wide rivulets all resemble the 5cm graph. The figure shows that narrow rivulets, shaped by surface tension, assume an approximately circular profile. As the width increases a flat zone develops in the centre, where gravity determines the shape and surface tension plays a significant role only near the edges.

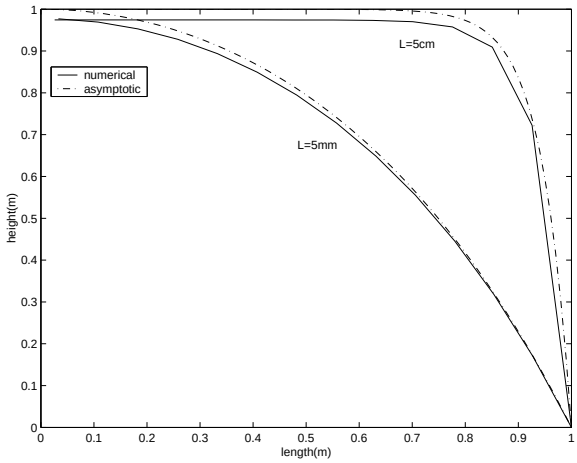

Figure 3.2: Rivulet cross sections for $L = 5mm, 5cm, \theta = 15^o$.

Figure (3.3) shows a comparison of the numerical and asymptotic results of the cross-sections of rivulets for different contact angles with $\alpha = 15^o$ and $L = 5mm$. The asymptotic results follow the leading order height, equation (2.19). With a contact angle $\theta = 15^o$ the two solutions are in good agreement, with a maximum error at $L = 0$ of approximately 3%. As the contact

angle increases, the solutions diverge. When $\theta = 40^o$ the maximum error increases to around 16%. This provides a guideline for when the asymptotic solution is valid.

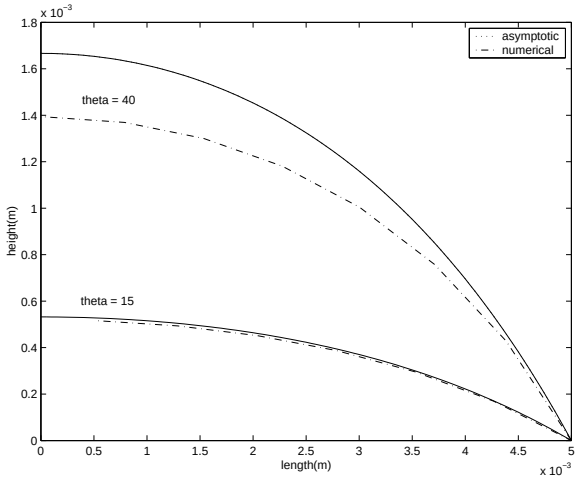

Figure 3.3: Rivulet cross sections for $L = 1cm, \theta = 15^o, 40^o$

Velocity contour

Next, we used the PDE toolbox in MATLAB to compute the velocity w given the PDE:

$$\Delta w = \frac{\rho g \sin \alpha}{\mu} \tag{3.12}$$

with boundary condition

$$w(x, 0) = 0$$

and continuity of tangential stress

$$\frac{\partial w}{\partial n} = \frac{T}{\mu}$$

at the free surface $y = h(x)$. The PDE toolbox automatically grids the specified domain and will subdivide the original grid for more accurate computations as requested. Numerical results are computed to at least 1% accuracy based on a refinement study. For example, in the $L = 1cm, \theta = 15^o$ rivulet computation, a total of 128 triangular grids are used in the domain to give this accuracy. The toolbox uses standard linear finite element method.

We consider two representative cases in the computations. One is the shear driven case ($T \neq 0, \alpha = 0$), and the other is the gravity driven case with zero shear ($T = 0, \alpha \neq 0$).

The asymptotic and numerical velocity contours are shown in Figures 3.4-3.11 below. The asympototic results follow equation (2.20). The axes of the asymptotic velocity contours are non-dimensional, while they are dimensional for the numerical values. However, the velocity contour values are dimensional for both asymptotic and numerical computations. In addition, velocity contours of only half of the rivulet are shown for the asymptotic computations, while the contours are shown for the whole rivulet for the numerical ones. One important thing to notice is that the velocity values obtained from the asymptotic formula and those obtained from the numerical calculations are very close to each other. However, this is not the case for fluxes and energies which will be shown later.

The parameter values used in the computations are:

- ρ: density of water $(1000kg/m^3)$
- μ: viscosity of water $(1.0 * 10^{-3}kg/m/s)$
- σ: surface tension between water and air $(72.4 * 10^{-3}kg/s^2)$
- g: gravity acceleration $(9.81m/s^2)$
- α: angle of inclination (15^o)

For the $5mm$ rivulet, velocity contours for zero inter-facial shear are shown in Figures 3.4 and 3.5. The velocities decrease from a maximum of -0.5 (i.e. in the direction of gravity) at the apex to 0 at the substrate. The velocity contour values are negative since the flow is driven by gravity which is in the negative direction. Note, that at the liquid-gas interface, the contour lines are almost vertical, in keeping with the condition $\partial w/\partial y = T + O(\epsilon^2) \approx 0$.

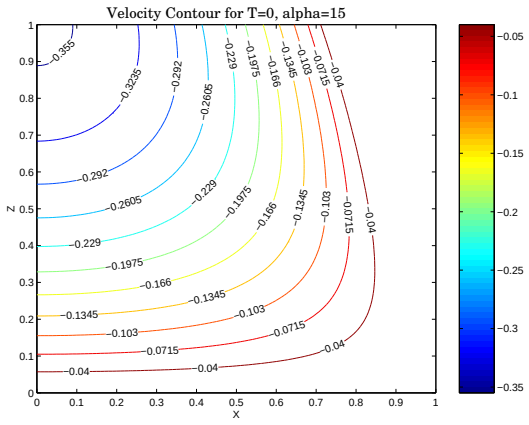

Figure 3.4: Asymptotic velocity contours in m/s for $L = 5mm, T = 0, \theta = 15^o$

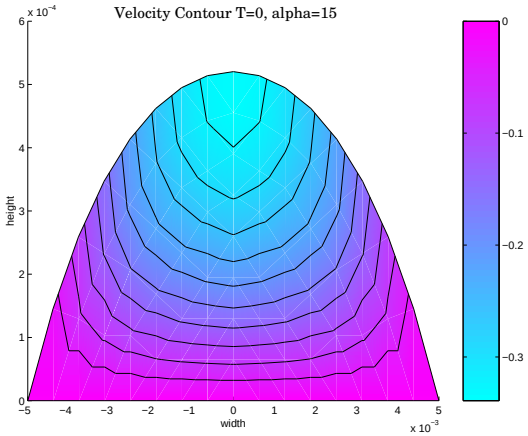

Figure 3.5: Numerical velocity contours in m/s for $L = 5mm, T = 0, \theta = 15^o$

If the inter-facial shear is increased, then the surface components of the fluid will move against gravity, and a sufficiently high values of T pushes all the fluid against gravity. This resembles the familar situation of rivulets being blown up the windscreen of a fast moving car. On Figure 3.6 and 3.7 an example is shown with relatively low shear ($T = 0.5$), so the central part of the rivulet moves with gravity. The zero velocity contour, which starts at the apex, can be seen to split the rivulet; at the edges the fluid flows in the direction of the air, near the centre gravity dominates and the flow is down the plane.

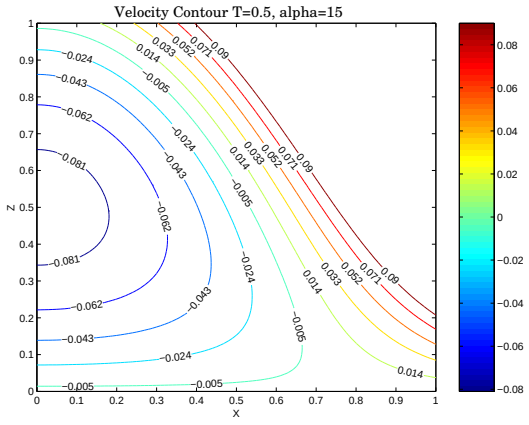

Figure 3.6: Asymptotic velocity contours in m/s for $L = 5mm, T = 0.5, \theta = 15^o$

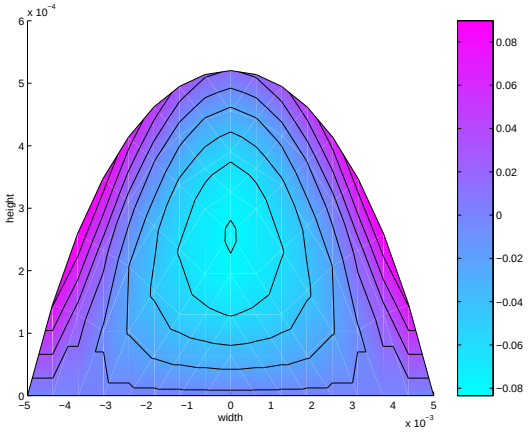

Figure 3.7: Numerical velocity contours in m/s for $L = 5mm, T = 0.5, \theta = 15^o$

Increasing T further the gravity driven region becomes smaller and finally disappears. Subse-

quently the velocity contours become much flatter, approaching that of a thin sheet rather than a rivulet, i.e. the velocity $w \approx w(y)$. Increasing T further strengthens this effect, until the x dependence becomes negligible, except for in a boundary layer at the rivulet edge. A sample is shown in Figures 3.8 and 3.9 for $T = 1$.

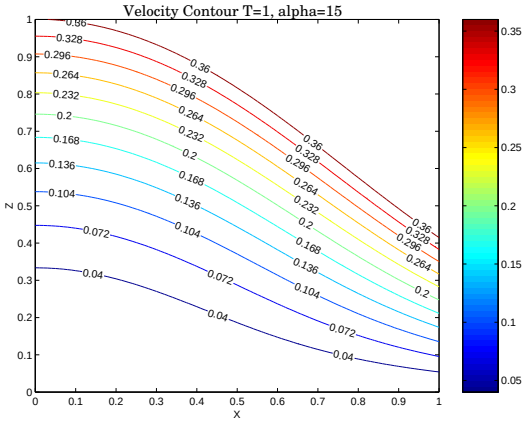

Figure 3.8: Asymptotic velocity contours in m/s for $L = 5mm, T = 1, \theta = 15^o$

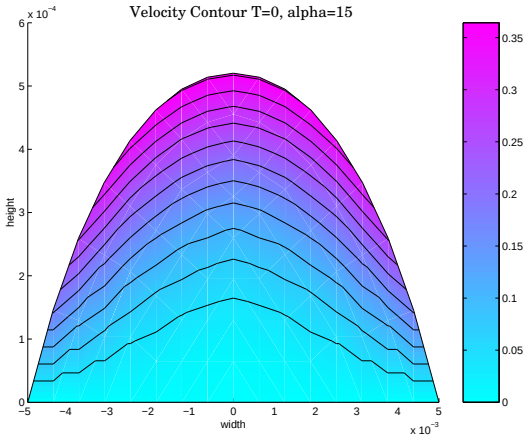

Figure 3.9: Numerical velocity contours in m/s for $L = 5mm, T = 1, \theta = 15^o$

For $T < 0$, i.e. negative shear stress, which is in the same direction as gravity, we expect larger negative velocity values compare with zero shear stress case. For example, with $T = -1$, the maximum negative velocity is -1.0, as shown in Figures 3.10 and 3.11.

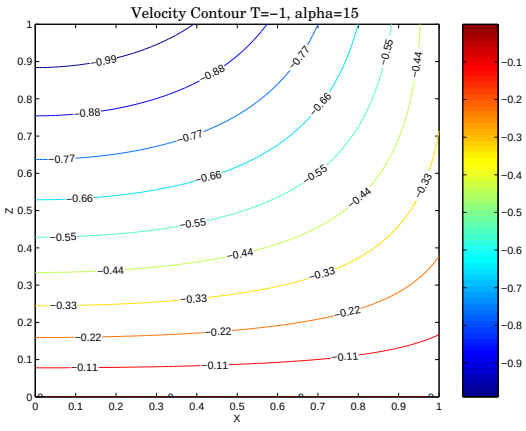

Figure 3.10: Asymptotic velocity contours in m/s for $L = 5mm, T = -1, \theta = 40^o$

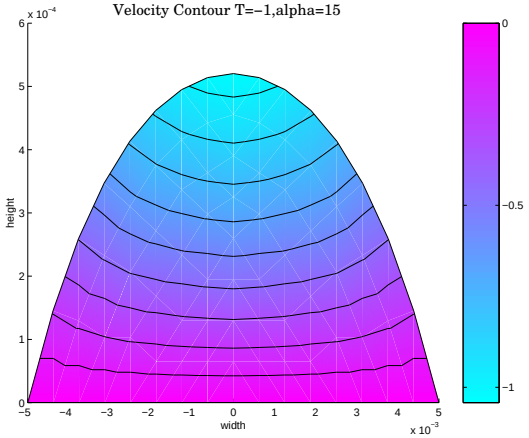

Figure 3.11: Numerical velocity contours in m/s for $L = 5mm, T = -1, \theta = 40^o$

Flux and energy

The asymptotic and numerical flux results are shown in Figures 3.12-3.15 as a function of rivulet length L. The asymptotic flux follows equation (2.25).

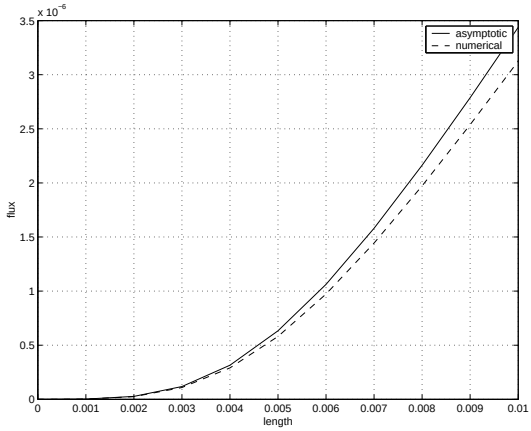

Figure 3.12: Flux of rivulet for $L = 1cm, T = 0, \alpha = 15^o, \theta = 15^o$

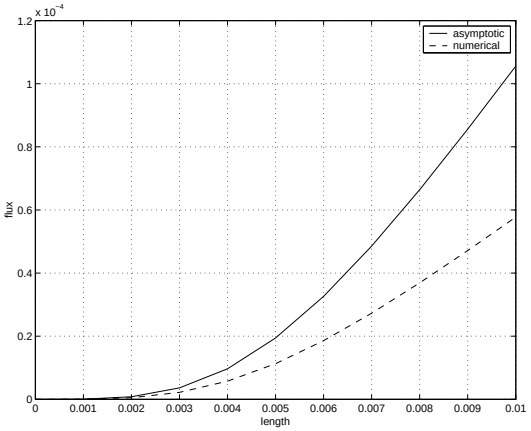

Figure 3.13: Flux of rivulet for $L = 1cm, T = 0, \alpha = 15^o, \theta = 40^o$

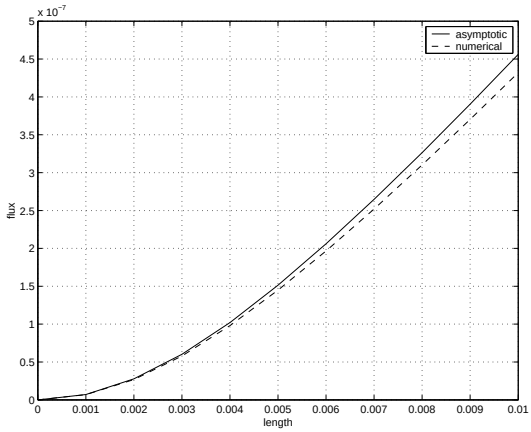

Figure 3.14: Flux of rivulet for $L = 1cm, T = 1, \alpha = 0, \theta = 15^o$

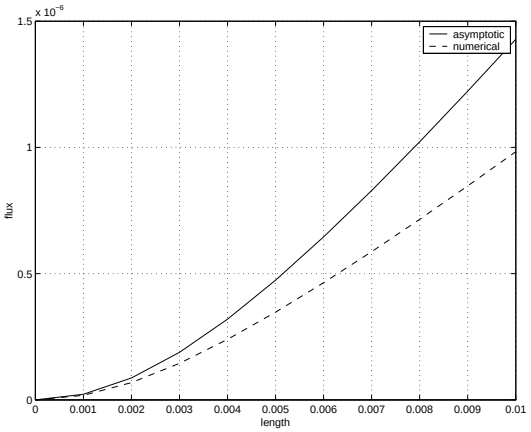

Figure 3.15: Flux of rivulet for $L = 1cm, T = 1, \alpha = 0, \theta = 40^o$

In Figure 3.12 the flux variation with width is shown for a rivulet driven solely by gravity, with a contact angle $\theta = 15^o$. The two curves are very close but slowly diverging as L increases. In this case the maximum half-width is $1cm$, at which stage the percentage difference between the curves is 9.98%. In Figure 3.13 the contact angle increases to 40^o. The two curves diverges much faster compare to Figure 3.12. This shows strong dependence of θ value in the asymptotics.

Figures 3.14 and 3.15 show the flux curves for an inter facial shear driven rivulet ($T = 1$) with the contact angle taking values of $\theta = 15^o, 40^o$. In each case the curves diverges with increasing length. When $\theta = 15^o$ the maximum error is around 0.4%, and the maximum error increases to 11.3% for $\theta = 40^o$.

The energy results as a function of length L are shown below in Figures 3.16-3.19. The asymptotic energy follows equation (2.37).

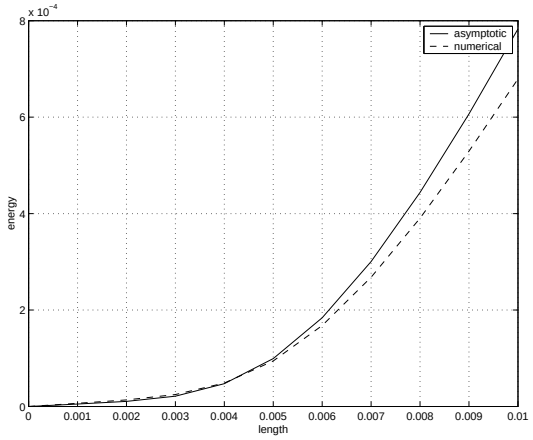

Figure 3.16: Energy of rivulet for $L = 1cm$, $T = 0, \alpha = 15, \theta = 15^o$

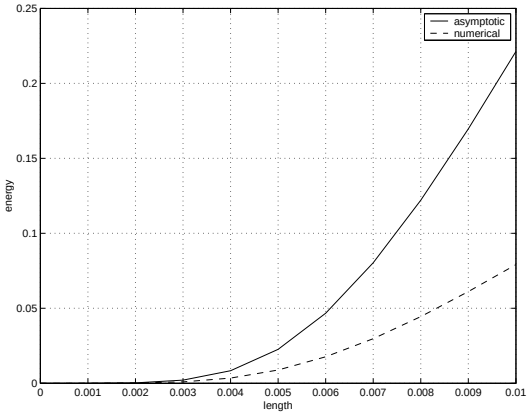

Figure 3.17: Energy of rivulet for $L = 1cm, T = 0, \alpha = 15, \theta = 40^o$

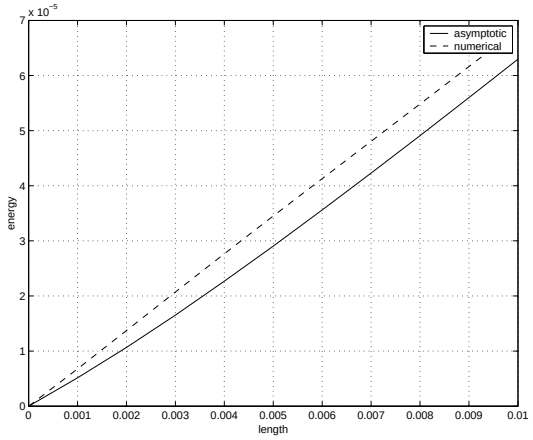

Figure 3.18: Energy of rivulet for $L = 1cm, T = 0, \alpha = 0, \theta = 15^o$

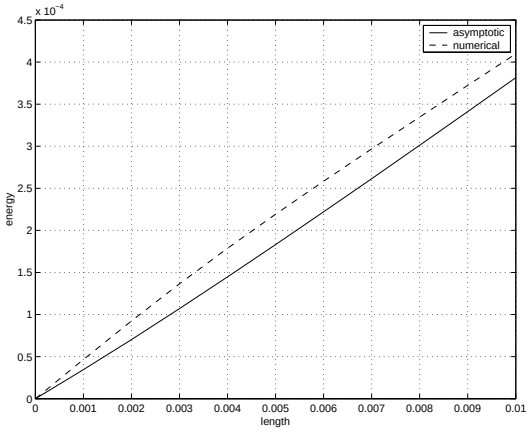

Figure 3.19: Energy of rivulet for $L = 1cm, T = 1, \alpha = 0, \theta = 40^o$

The curves resembles the curves of flux vs. length for the gravity driven energy plot (Figures

3.16 and 3.17), i.e. the error increases with increasing length and θ value.

However, the results are not quite as expected for the shear driven case (Figures 3.18 and 3.19). The error diverges as length increases up to a critical value around $L = 3mm$, then there seems to be a constant offset between asymptotic energy and numerical energy as L increases further. This is due to the fact that surface energy is dominant when there is no gravity, which is proportional to length L of the rivulet for L large.

3.2 Stability Analysis Based On Energy Criterion

In 1990, P.Schmuki and M.Laso [3] studied the stability of rivulet flow using a simplified rivulet model, i.e. treating the shape of the rivulet as a circular arc. The model is based on an energy criterion: the rivulet ceases to be stable when the total energy of the single rivulet can be lowered by its decaying into several smaller ones (subrivulets). The strategy is to formulate the total energy of the system and then to find the minimum value of this energy as a function of the number of sub-rivulets for a given total flow rate.

We will borrow the idea and study the stability of a single rivulet vs. two sub-rivulets. For a rivulet of a specified flux Q, it will be unstable to breakup into two smaller rivulets if

$$E(Q) > E(Q - q) + E(q)$$

for some $0 < q < Q$. We denote by Q_c the minimum of all such fluxes Q allowing energetically favorable breakup and let L_c be the corresponding rivulet length. Clearly then, rivulets of length less than L_c are stable to breakup and those with length greater than L_c are unstable.

For gravity driven, zero shear flow, we compute the rivulet energy as a function of flux as shown in Figures 3.20 and 3.21. Note that $E \propto Q$ for large L and the dependence of E and $Q^{1/4}$ for small L can be seen clearly from the plots. But we should expect $E \propto Q^{1/4}$ as predicted by asymptotic analysis in chapter 2.

For the shear driven and no gravity flow, the energy vs. flux results are shown in Figures 3.22 and 3.23. The qualitative behaviour also fits our asymptotic analysis in chapter 2, i.e. $E \propto Q^{1/3}$

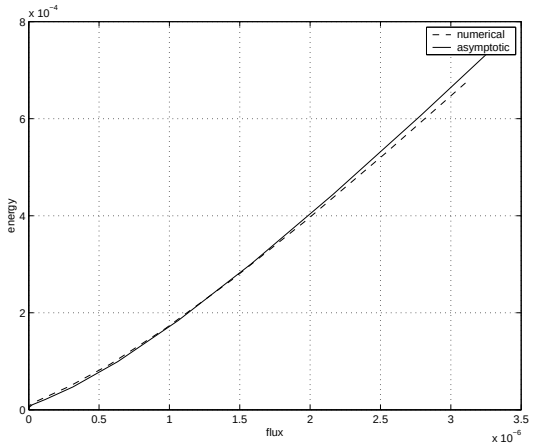

Figure 3.20: Energy vs. flux of rivulet for $L = 1cm, T = 0, \alpha = 15, \theta = 15^o$

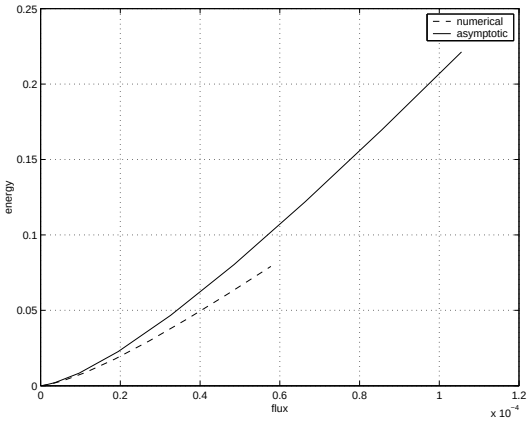

Figure 3.21: Energy vs. flux of rivulet for $L = 1cm, T = 0, \alpha = 15, \theta = 40^o$

for L small and $E \propto Q$ for large L.

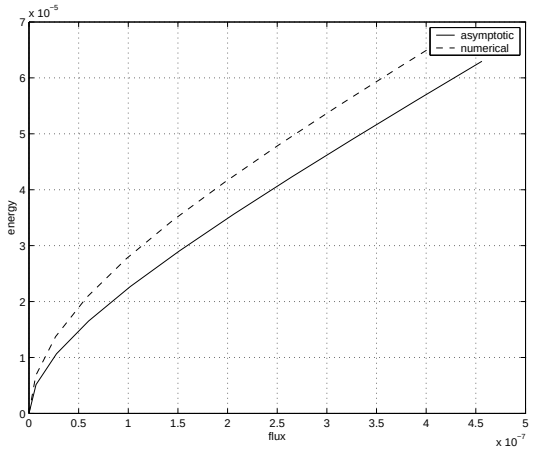

Figure 3.22: Energy vs. flux of rivulet for $L = 1cm, T = 1, \alpha = 0, \theta = 15^o$

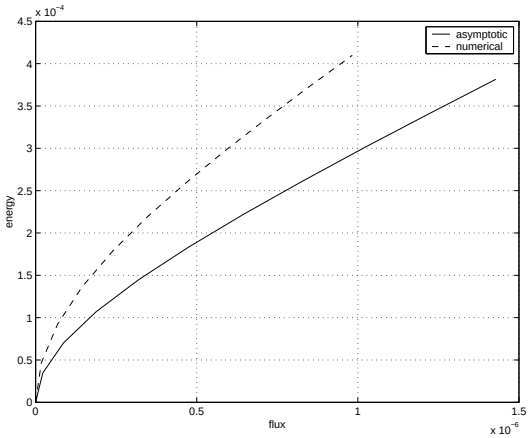

Figure 3.23: Energy vs. flux of rivulet for $L = 1cm, T = 1, \alpha = 0, \theta = 40^o$

Examine Figures 3.20-3.23, we notice that the concavity of the $E(Q)$ graph for the gravity driven case changes from concave up to concave down near the origin, while the graph is always concave down for the shear driven case. We can conclude that the gravity driven case has potential for breaking up into smaller rivulets, but it is never energetically favourable to break up into smaller rivulets for the shear driven rivulets. To be precise, we emphasize that only one kind of instability is considered in this analysis (break up into multiple rivulets) and that other

mechanisms (meander, breakup into droplets) could lead to instabilities in the shear driven case, and may lead to earlier instabilities in the gravity driven case.

Asymptotic inflection points

Since change of concavity leads to instability, and concavity changes at inflection points, we search for the inflection point using the asymptotic energy formula. Then we compute energies for different rivulet sizes to see if it is energetically favorable for a rivulet to break up. Since we only have formulas for E and Q as a function of L, and it is impossible to solve E as a function of Q explicitly due to the complexity of the equations, We apply the chain rule to find the inflection points which corresponds to Q values such that $E^{''}(Q) = 0$.
Since,

$$E^{''}(Q) = \frac{Q^{'}(L)E^{''}(L) - E^{'}(L)Q^{''}(L)}{(Q^{'}(L))^3} \tag{3.13}$$

so $E^{''}(Q) = 0 \Rightarrow$

$$Q^{'}(L)E^{''}(L) - E^{'}(L)Q^{''}(L) = 0 \tag{3.14}$$

Maple is used to do the root searching, and find that the inflection point occurs at about $L_c = 1.4mm$ for $\theta = 40^o$, and $L_c = 2.67mm$ for $\theta = 15^o$ for the gravity driven case. This indicates that rivulet is more stable for small contact angles since the inflection point occurs at larger values of L. This is what we expected. Next we go on to find the critical point where the rivulet breaks.

Numerical and asymptotic critical points

We did a spline fit using the data E(a) and Q(a) (both numerical and analytical data) to obtain an numerical approximation of the function $E(Q)$. Then we divide Q into N equally spaced intervals, and compute $E(Q_i)$ for each $Q_i, i = 1 \cdots N$. The inflection point Q_I at specific L_c was located. Starting from Q_{I+1} upwards we searched for the smallest critical flux Q_c such that the following equation is satisfied:

$$Q_c = \inf\{Q : E(Q) > E(q) + E(Q - q), 0 \leq q \leq Q\} \tag{3.15}$$

θ	method	Q_c	L_c
10^o	asymptotic	4.9513e-07	7.3mm
	numerical	6.6490e-07	8.5mm
15^o	asymptotic	3.0942e-07	4.0mm
	numerical	5.0016e-07	4.8mm
20^o	asymptotic	5.3161e-07	3.6mm
	numerical	7.2570e-07	4.1mm
30^o	asymptotic	6.4747e-07	1.9mm
	numerical	9.1391e-07	1.9mm
40^o	asymptotic	8.5269e-07	3.3mm
	numerical	1.1602e-06	4.5mm
45^o	asymptotic	7.6853e-07	1.9mm
	numerical	1.1721e-06	2.5mm

Table 3.1: Numerical estimates of Q_c and L_c for gravity driven rivulet.

For the gravity driven case, the critical flux Qc and the corresponding critical length Lc for $\theta = 15^o$ and $\theta = 40^o$ are listed in table 3.1.The data shows that both Q_c and L_c get smaller as θ increases. Thus rivulets with bigger contact angles are more likely to break up than rivulets with smaller contact angles, which makes sense.

Chapter 4
Combined Air and Rivulet Flow

Two-phase flow can exist in a variety of regimes, such as bubbly flow, slug flow, churn flow, and annular flow. This is described in detail by Fowler[13]. Fowler also introduced a flow regime map, which classifies the flow patterns according to density, velocity, and gas volume fractions. However, this classification doesn't include the case of the two-phase flow in a typical small dimensional fuel cell. Those fuel cells are in the order of 1mm diameter, and the velocity of flow is typically in the order of $1m/s$ for air and $10^{-4}m/s$ for water. So we propose a new model to study the flow inside a fuel cell.

We model the fuel cell channel as a circular pipe with a given diameter and study the flow in 2-D. We also assume that the flow is in rivulet form. For a small rivulet with a small capillary number (equals to 0.14 for $L = 1mm$), pressure and surface tension are the dominant forces that affect the motion of a rivulet. Gravity can be ignored to simplify the computation. First, we do the direct problem, i.e. compute the fluxes of the coupled water/air flow for a given pressure gradient and configuration. Then we do the inverse problem, where fluxes are given, and we compute the pressure gradient needed to drive the flow and configuration of the rivulet. Then we apply the problem to a specific situation, modeling water movement inside a fuel cell.

Many different aspects of research have been done to understand the science behind a proton exchange membrane(PEM) fuel cell. Such as gas flow in the electrodes, gas flow with condensation and other thermal effects, and liquid (water) motion driven by air flow. One aspect that affects the performance of PEM fuel cells is the accumulation of liquid water in the oxygen channel. Presence of certain amount of water is necessary for ionic transportation in the

membrane. However, if there is too much water inside the electrodes, it could block the flow of oxygen, thus reducing the efficiency of the fuel cell. In some fuel cell designs, liquid water is pushed out into the channels with the flow of reactant gases. Thus, an understanding of the two phase (water and air) flow is essential to improve the performance of fuel cell.

The geometry of an idealized flow channel is shown in Figure 4.1. Following the same as-

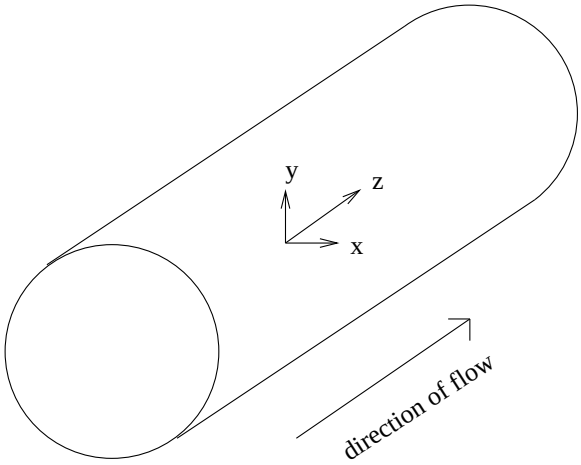

Figure 4.1: Geometry of a fuel cell channel.

sumptions listed in chapter 1 and neglect gravity in addition, the system is governed by $\vec{u} = (0, 0, w(x, y))$ with $p(z) = \lambda z$. Equation (1.1) becomes

$$\mu \Delta w - \lambda = 0 \tag{4.1}$$

Physically, the pressure drop along x-y direction is governed by equation (1.9). Since $G_2 = G_3 = 0$, we get

$$p_w - p_a = -\sigma k \tag{4.2}$$

where σ is the surface tension of water and h is the height of the rivulet. P_a is the air pressure and P_w is water pressure. Since gravity is ignored, the pressure drop in the x-y plane is constant. We get a constant curvature in the plane. Constant curvature corresponds to the geometry of circular arcs. Circular arcs exist in two states. One is the full circle which corresponds to annulus flow, and the other geometry is an arc of a circle which corresponds to circular arc flow. These two kinds of flows are investigated in detail below. But first we study the circular channel flow with only air in it.

4.1 Air Only Channel Flow

Assume there is no water present in the circular channel, we solve the poission equation $\mu_a \Delta w = \lambda$ in polar-coordinates with boundary condition $w = 0$. Let the radius of the channel be R. Then the velocity of air is:

$$W_a(r) = \frac{\lambda}{4\mu_a}(-r^2 + R^2) \tag{4.3}$$

To get the flux of air, we integrate the veloxity over the surface area, i.e.

$$Q_a = 2\pi\rho_a \int_0^R W_a(r) \cdot r dr \tag{4.4}$$

which gives us the following linear relationship between the pressure gradient and flux of air.

$$\lambda = \frac{8\mu_a}{\pi R^4 \rho_a} Q_a \tag{4.5}$$

Which agrees with the result of [6]. Next we allow both water and air coexist in the channel, and do a similar analysis.

4.2 Annulus Rivulet

First, assume the rivulet clings itself to the wall of the channel symmetrically, with air flowing down in the core as shown in Figure 4.2.

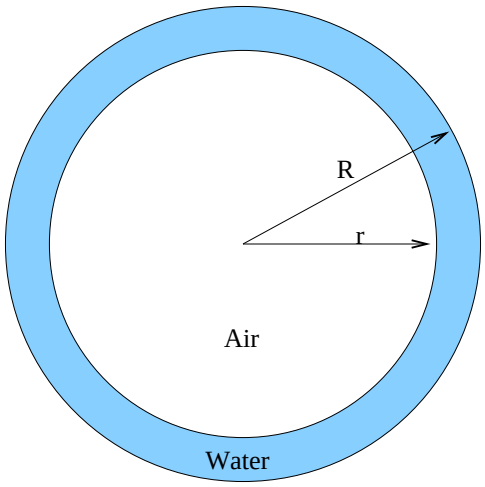

Figure 4.2: Cross section geometry of a ring rivulet channel.

Both the water and air domains are governed by similar equations, and by the same boundary conditions as for the air only case. We have $\mu_a \Delta w = \lambda$ in the air region, and $\mu_w \Delta w = \lambda$ in the water region. Together with the boundary and interface conditions below

Boundary Condition: $w = 0$

Interface Condition: $[w] = 0$ and $[\mu w_n] = 0$

we compute the velocity profile inside the channel. The interface conditions correspond to continuity of velocity and stress at the water-air interface γ. $[\cdot]$ denotes the difference in the quantities across the interface γ. And w_n is the normal velocity.

For a given channel size R, and radius of air flow $\hat{r}$, we find the velocity of air and water at radius r are:

$$W_a(r) = \frac{\lambda}{4\mu_w}(\hat{r}^2 - R^2) + \frac{\lambda}{4\mu_a}(r^2 - \hat{r}^2) \qquad (0 < r < \hat{r})$$

$$W_w(r) = \frac{\lambda}{4\mu_w}(r^2 - R^2) \qquad (\hat{r} < r < R)$$

Integrating velocity over the area of each corresponding domain, we get the fluxes of water and air.

$$\begin{aligned} Q_w &= \int_{\hat{r}}^{R} W_w(r) 2\pi r dr \\ &= \pi \rho_w \lambda \left[\frac{R^4 - \hat{r}^4}{8\mu_w} - \frac{R^2(R^2 - \hat{r}^2)}{4\mu_w} \right] \end{aligned}$$

$$\begin{aligned} Q_a &= \int_{0}^{\hat{r}} W_a(r) 2\pi r dr \\ &= \pi \rho_a \lambda \left[\frac{\hat{r}^4}{8\mu_a} + \frac{1}{4} \left(\left(\frac{1}{\mu_w} - \frac{1}{\mu_a} \right) \hat{r}^2 - \frac{R^2}{\mu_w} \right) \hat{r}^2 \right] \end{aligned}$$

We are interested in the relationship between pressure gradient and water flux for fixed air flux. To find it, we will compute the fluxes up to leading order for small $h = R - \hat{r}$ and fixed gas

flux.

$$\begin{aligned} Q_w &= \int_{R-h}^{R} W_w(r) 2\pi r dr \\ &= -\frac{R^2 \pi \lambda}{2\mu_w} h^2 + O(h^3) + \cdots \end{aligned}$$

$$\begin{aligned} Q_a &= \int_{0}^{R-h} W_a(r) 2\pi r dr \\ &= -\frac{\pi \lambda}{2}[-\frac{R^4}{4\mu_a} + (\frac{R^3}{2\mu_w} + \frac{R^3}{4\mu_a})h + O(h^2) + \cdots] \end{aligned}$$

Let $C_1 = -\frac{R^4}{4\mu_a}$ and $C_2 = \frac{R^3}{2\mu_w} + \frac{R^3}{4\mu_a}$, write $\lambda = \lambda_o + \lambda^{'}$ where λ_o is the base solution, and $\lambda^{'}$ is a small pertubation from the base solution. Then a linear analysis for small h gives:

$$\begin{aligned} Q_a &= \frac{\pi}{2}(\lambda_o + \lambda^{'})(C_1 + C_2 h + \cdots) \\ &= \frac{\pi}{2}(\lambda_o C_1 + \lambda^{'} C_1 + \lambda_o C_2 h + \cdots) \end{aligned}$$

For fixed air flux, the last two terms must cancel. Thus we have $\lambda^{'} \propto h$. Since $Q_w \propto h^2$, we get the pressure gradient increases as the square root of the increase in water flux, i.e.

$$\lambda^{'} \propto \sqrt{Q_w^{'}} \tag{4.6}$$

4.3 Circular Arc Rivulet

For the case that water accumulates at the botom of the channel, we assume it forms a rivulet with circular arc interface there, shown in Figure 4.3. θ is the contact angle, and ψ is the angle that determines the size of the circular arc.

The governing equations are the same as the annulus rivulet case, except that the geometry is different. Since there is no analytic equations to describe the flow field w as a function of θ and ψ, we are not able to solve the coupled problem analytically. Instead, we used a software package called FEMLAB to calculate the velocity profile. FEMLAB allows the user to specify the geometry and the PDEs to be solved, together with boundary and interface conditions. Then it generates triangular meshes and uses finite element method to solved the PDE. Figure 4.4 below shows the meshes generated by FEMLAB after refinement.

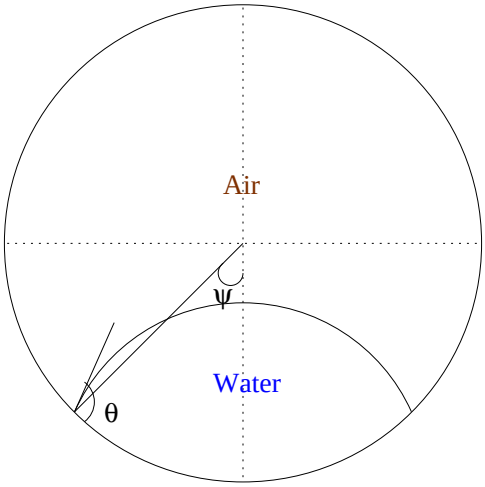

Figure 4.3: Cross section of a circular arc rivulet channel.

4.3.1 The direct problem

First we solve the direct problem. i.e. with ψ and λ given, find the size of the rivulet, compute the velocities of water and air, and then integrate to get the fluxes.

The following data are used in the calculations.

- $\mu_a = 1.8 * 10^{-5}$ kg/m/s
- $\mu_w = 1.0 * 10^{-3}$ kg/m/s
- Radius of channel: 1 mm
- Pressure gradient: 100 Pa/m
- Contact angle (θ): 84^o (between graphite and water)[10]

The velocity contours are shown in figure 4.5. Notice that the velocity contours have different slopes at the interface due to continuity of shear stress and the difference in viscosity of air and water. The numerical solutions given by FEMLAB are verified using a simpler rectangular geometry where analytical solutions can be obtained easily. (see Appendix for details)

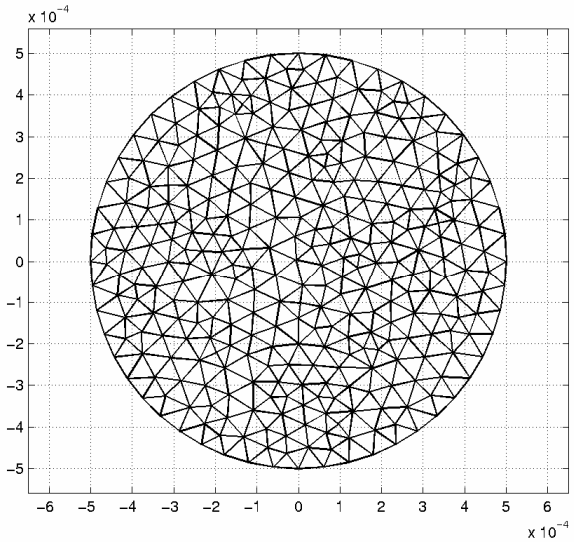

Figure 4.4: Triangular mesh of the cross section domain

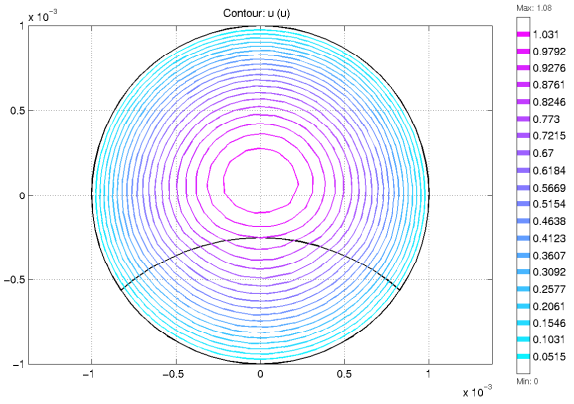

Figure 4.5: Contour plot of fluxes

4.3.2 The inverse problem

The inverse problem is: given fluxes of air(Q_a), water (Q_w) and size of the channel R, determine the size of the rivulet (ψ) and the pressure gradient (λ) needed to drive the flow.

Consider the general equation $\mu \Delta w = \lambda$. Let $x \to L\hat{x}$, $y \to L\hat{y}$, where $\hat{x}$ and $\hat{y}$ are nondimensional quantities. Thus

$$\Delta w = \frac{\partial^2 w}{\partial x^2} + \frac{\partial^2 w}{\partial y^2} = \frac{1}{L^2}(\frac{\partial^2 w}{\partial \hat{x}^2} + \frac{\partial^2 w}{\partial \hat{y}^2})$$

Since $Q = \int w dA$, for fixed Q, we have λ varies like $1/r^4$. (A factor of $1/r^2$ comes from w

and another factor of $1/r^2$ comes from A, the area of the cross section). For computational simplicity, let $R = 1$, and also $\lambda = 1$. We will use $\lambda = 1$ and $R = 1$ in our proceeding calculations of the reference water and air fluxes.

Note that the equation $\mu \Delta w = \lambda$ is linear in λ. This property is exploited below to reach a scalar inverse problem. The computation is carried out in the following steps:

1. Based on the radius(R) of the channel and contact angle(θ) between water and the channel, calculate the size of the rivulet that gives $Q_{ratio} = \frac{Q_a}{Q_w}$ using $\lambda = 1$ and $R = 1$ by modifying the angle ψ in successive iterations, and terminate when the specified error tolerance is reached.

2. Use either equation $\lambda = \frac{Q_a(target)}{r^4 Q_a(\lambda=1)}$, or $\lambda = \frac{Q_w(target)}{r^4 Q_w(\lambda=1)}$ to calculate the pressure gradient and fluxes for the specified channel size and contact angle.

Next we apply the method above to a specific case. Suppose we have a 1mm diameter circular channel with length 1m. Then the effective area of the channel is diameter times length, which $10cm^2$. Also suppose the current density is $1A/cm^2$, then the total current goes through the channel is $10C/s$. The electro-chemistry inside the fuel cell is governed by:

$$H_2 \rightarrow 2H^+ + 2e^-$$

$$O_2 + 4e^- + 4H^+ \rightarrow 2H_20$$

Thus 1 mole of water corresponds to 2 moles of electron. The current I corresponds to $I/2F$ moles of water, where F is the Faraday's constant ($9.632 * 10^4 C/mol$). The flux of water is: $Q_w = 18 * 10/2F kg/s$, and 18 is the molar mass of water. The flux of air is: $Q_a = (32 + .78/.21 * 28) * 2 * 10/4F kg/s$, where 32 is the molar mass of oxygen and 28 is the molar mass of nitrogen, and Oxygen occupies 21% of the volume in air and nitrogen occupies 78%. Other small percentage of gases that makes the air composition are neglected. 2 is the usual stoichiometric flow factor which is the ratio of the amount of input air to the minimum amount of air needed for reaction. So the targeting fluxes of air and water are:

$$Q_w = 9.3 * 10^{-4} kg/s$$

Table 4.1: Pressure gradient λ(Pa/m) and size of rivulet for different channel sizes

θ	**R**			ψ
	1mm	0.5mm	0.25mm	
60^o	$\lambda = 2.83248e+01$	$\lambda = 4.529674e+02$	$\lambda = 7.2475e+03$	17.5^o
84^o	$\lambda = 2.82130e+01$	$\lambda = 4.506544e+02$	$\lambda = 7.2105e+03$	12^o
100^o	$\lambda = 2.82906e+01$	$\lambda = 4.526498e+02$	$\lambda = 7.2424e+03$	10^o

$$Q_a = 7.1 * 10^{-3} kg/s$$

Using these data, we find that the ratio of flux of air and water is: $Q_{ratio} = \frac{Q_a}{Q_w} = 7.6$.

FEMLAB is used to carry out the steps 1-3 above, and compute the results in Table 4.1. The data shows that λ(pressure drop) is more sensitive to change in size of channel(radius) than to change in contact angle.

Figures 4.6 and 4.7 show rivulet sizes for different specifications of contact angle and radius of channel. The rivulet is concave in Figure 4.6, and convex in Figure 4.7. The qualitative shape of a rivulet depends on a number of factors. For example, the contact angle between water and the channel, radius of the channel and the flux ratio. Notice that the velocity contours of water are not shown in Figure 4.7. This is because the velocity of water is much smaller than the velocity of air.

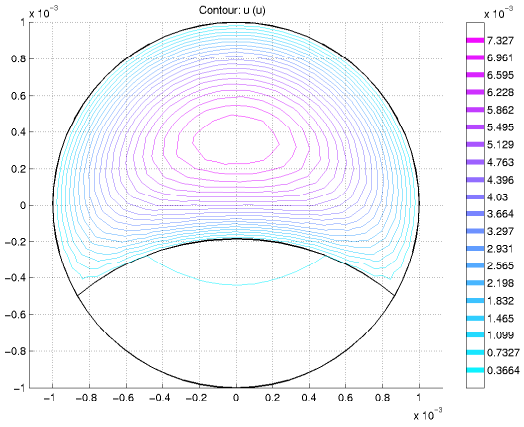

Figure 4.6: shape of rivulet for r=1mm, $\theta = 100^o$.

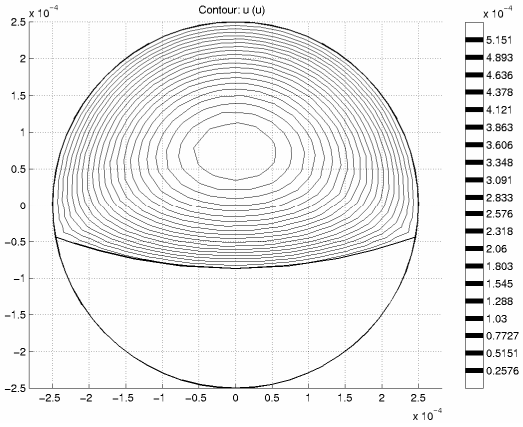

Figure 4.7: shape of rivulet for r=.25mm, $\theta = 60^o$.

In an actual fuel cell, fluxes vary down the channel. It will be more useful from a practical point of view that we have a way to find the pressure gradient for an arbitrary Q_{ratio}. So we get the following universal curves. Figure 4.8 gives rivulet size ψ for any Q_{ratio}, and Figure 4.9 gives the air flux (Q_a^*) for $\lambda = 1$. With this information, we can estimate the pressure gradient for an arbitrary given air flux Q_a and radius r of the channel, i.e.

$$\lambda = \frac{Q_a}{Q_a^* \cdot r^4} \tag{4.7}$$

Engineers could use these universal curves to recompute each specific configuration down each unit section of the channel and integrate the local pressure gradient to obtain an approximation of the net pressure drop down the channel.

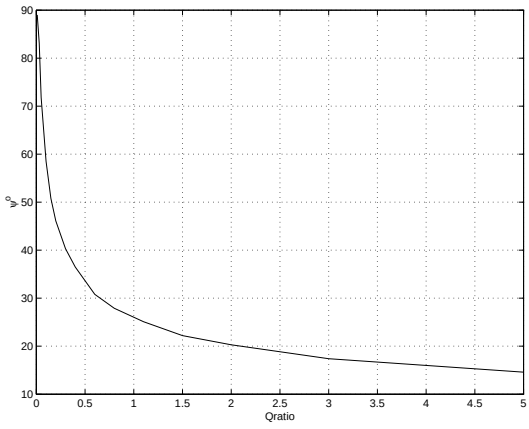

Figure 4.8: Rivulet size ψ vs. Q_{ratio} for R=1mm, $\theta = 84^o$.

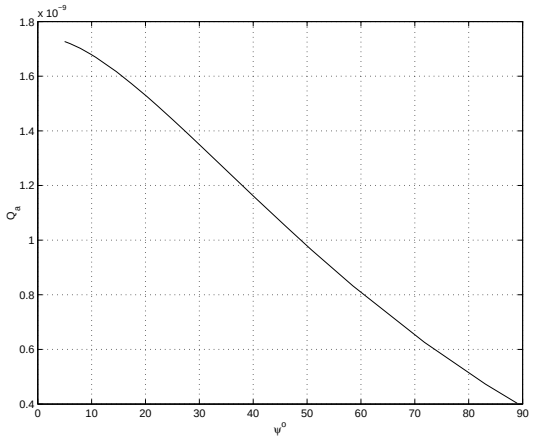

Figure 4.9: Air flux vs. ψ for R=1mm, $\theta = 84^o$, and $\lambda = 1$.

4.4 Pressure gradient vs. flux of water

We know that $\lambda \approx C_1\sqrt{Q_w}$ up to leading order for relatively small Q_w with Q_a fixed for annulus rivulet from asymptotic analysis, as indicated in equation (4.6). However, it is impossible to get asymptotic results for the circular arc rivulet due to algebraic complexity of the problem. So we did a comparision of pressure gradient vs. flux of water of the two cases numerically, and the results are shown in Figure 4.10.

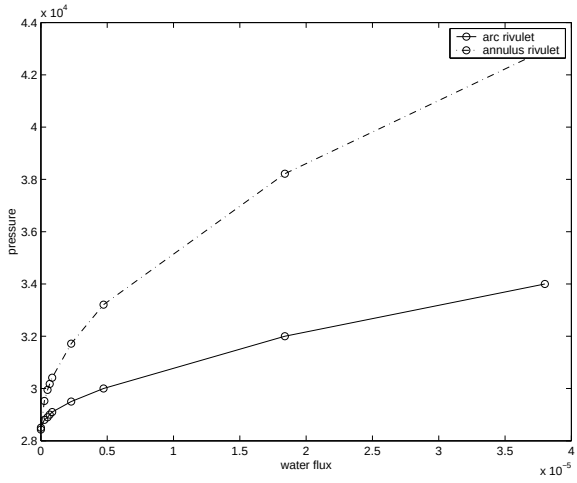

Figure 4.10: Pressure gradient vs. Qw for annulus and circular arc rivulet

We conclude that the pressure gradient of the annulus model is more sensitive to change in

water flux than that of the circular arc model, but the qualitative behaviours are similar.

Chapter 5
Stability Analysis of Combined Air and Rivulet Flow

5.1 Stability of the annulus model

The stability of a steady, axisymmetric, laminar, nondiffusive, primary flow composed of two fluids flowing concentrically in a straight circular tube has already been investigated by Hickox[8]. The stability of the flow is determined by the method of small perturbations. Both axisymmetric and asymmetric disturbances to the primary flow are considered. Only infinitesimal disturbances to the primary flow are considered; hence, the analysis is a linear stability analysis. He found that the parallel flow is always unstable in the sense that a small perturbation to the flow will initially grow with time at an exponential rate, regardless of the size of the Reynolds number. It was found that the most important single cause of instability is the difference in viscosity between the fluid regions. Density variation and surface tension have less pronounced effects. However, only long wave numbers are considered in his analysis.

5.2 Linear stability of a rectangular geometry

There has been no study of the stability of our arc rivulets. A full scale analysis of the circular model is quite complicated and numerically involved. We will formulate a linear stability analysis of the free boundary coupled flow in a simple two dimensional rectangular domain instead to get the flavour of the technique, which could be applied to the computational stability analysis of the arc rivulet.

Consider water flows down the unbounded channel in x-direction in region 1 with viscosity μ_w, and air flows in region 2 with viscosity μ_a.

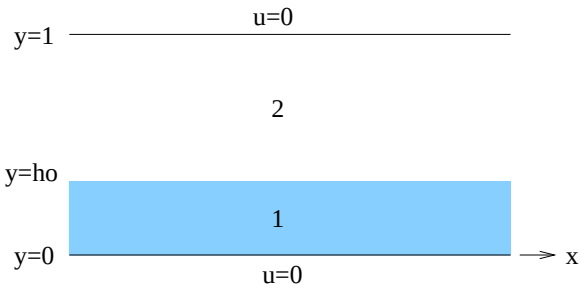

Figure 5.1: rectangular geometry

Steady state

Given the pressure gradient λ and the height of water h_o, we can calculate the velocity profile in the two regions for a steady state flow. The flow is governed by steady state equation:

$$\mu\nabla^2\vec{u_o} = \nabla p_o = (-\lambda, 0), \tag{5.1}$$

where

$$\vec{u_0} = (u_0(y), 0).$$

Integrate (5.1) with

$$\vec{u_0} = 0 \quad on \quad y = 0, 1. \tag{5.2}$$

then

$$u_{01} = Ay - \frac{\lambda}{\mu_w}y^2, \tag{5.3}$$

$$u_{02} = B(y-1) + \frac{\lambda}{\mu_a}(y-1)^2, \tag{5.4}$$

$$p_0 = -\lambda x. \tag{5.5}$$

where A and B are determined by

$$u_{01}(h_o) = u_{02}(h_0), \tag{5.6}$$

$$\mu_w\frac{\partial u_{01}}{\partial z}(h_o) = \mu_a\frac{\partial u_{02}}{\partial z}(h_0). \tag{5.7}$$

Solve the system and get

$$A = \frac{\mu_a}{\mu_w} B, \tag{5.8}$$

$$B = \frac{C}{h_0 - 1 - \frac{\mu_a}{\mu_w} h_0}, \tag{5.9}$$

$$C = \frac{\lambda}{2} h^2 (\frac{1}{\mu_a} - \frac{1}{\mu_w}) - \frac{\lambda}{2\mu_a}. \tag{5.10}$$

Linearized perturbation

Introduce a small perturbation to the steady state solution by writing $\vec{u} = \vec{u_0} + \vec{u_1}$, where $\vec{u_1} = (u_1, v_1)$, and $p = p_o + p_1$. Then substitute into the Navier-Stoke equation (1.1), ignoring external forces (including gravity), i.e.

$$\rho \frac{\partial \vec{u}}{\partial t} + (\vec{u} \cdot \nabla)\vec{u} = \mu \nabla^2 \vec{u} - \nabla p, \tag{5.11}$$

where

$$(\vec{u} \cdot \nabla)\vec{u} = (uu_x + vu_y, uv_x + vv_y). \tag{5.12}$$

Substitute and remove higher order terms, get the linearized system for $\vec{u_1}$

$$\rho \begin{pmatrix} u_{1t} \\ v_{1t} \end{pmatrix} + \begin{pmatrix} u_0 u_{1x} + v_1 u_{0y} \\ u_0 v_{1y} \end{pmatrix} = \mu \begin{pmatrix} \nabla^2 u_1 \\ \nabla^2 v_1 \end{pmatrix} - \begin{pmatrix} p_{1x} \\ p_{1ty} \end{pmatrix}. \tag{5.13}$$

Dispersion relation

We are interested in how the small disturbance $\vec{u_1}$ grows in time. Experience with the method of separation of variables and Laplace transforms suggests that the general solution can be expressed in terms of:

$$\vec{u_1} = \vec{u}_1(y) e^{ikx + \sigma t} \tag{5.14}$$

$$h_1 = h_1(y) e^{ikx + \sigma t} \tag{5.15}$$

$$\vec{p_1} = \vec{p}_1(y) e^{ikx + \sigma t} \tag{5.16}$$

We are interested in knowing the sign of σ in solving these equation. If $\sigma > 0$, the disturbance will be amplified, growing exponentially with time until it is so large that nonlinearity becomes

significant. Then nonlinear stability analysis will be compulsory. If $\sigma = 0$, it is said to be neutrally stable. And if $\sigma < 0$, it is said to be stable or asymptotically stable since the disturbance will remain small for all time. Since $\sigma = \sigma(k)$, where k is called the mode of the disturbance wave or the wave number, and it is generally true that a small disturbance of the basic flow will excite all modes, if $\sigma < 0$ for at least one mode then the flow is unstable. This analysis follows the method of normal modes described in Drazin [7].

Analysis

Substitute 5.14-5.16 into (5.13), get

$$ik u_1 + v_1^{'} = 0 \tag{5.17}$$

$$\sigma\rho u_1 + ik u_0 u_1 + v_1 u_0^{'} = \mu(-k^2 u_1 + u_1^{''}) - ikp_1 \tag{5.18}$$

$$\sigma\rho v_1 + u_0 v_1^{'} = \mu(-k^2 v_1 + v_1^{''}) - p_1^{'}. \tag{5.19}$$

with $u_1 = v_1 = 0$ on $y = 0, 1$.

Specifically, $u_{11}, u_{12}, v_{11}, v_{12}$ should satisfy the following linearized boundary and interface conditions. $u_{i,j}$ denotes velocity component u in region $j (j = 1, 2)$ with $i = 0, 1$ indicating the base solution and the perturbed solution.

1. No slip condition at the boundary:

$$\vec{u}(0) = 0 \Longrightarrow u_{11}(0) = v_{11}(0) = 0 \tag{5.20}$$

$$\vec{u}(1) = 0 \Longrightarrow u_{12}(1) = v_{12}(1) = 0 \tag{5.21}$$

2. Continuity of velocity at interface:

$$\vec{u_1}(h) = \vec{u_2}(h) \Longrightarrow \begin{cases} v_{11}(h_0) = v_{12}(h_0) \\ u_{11}(h_0) + h_1 u_{01}^{'}(h_0) = u_{12}(h_0) + h_1 u_{02}^{'}(h_0) \end{cases} \tag{5.22}$$

3. Continuity of shear stress:

$$\mu_1 \frac{\partial u_{i1,\tau}}{\partial n}(h) = \mu_2 \frac{\partial u_{i2,\tau}}{\partial n}(h) \tag{5.23}$$

$$\Longrightarrow \mu_1(u_{11}^{'}(h_0) + h_1 u_{01}^{''}(h_0)) = \mu_2(u_{12}^{'}(h_0) + h_1 u_{02}^{''}(h_0)) \tag{5.24}$$

Derivation:

$$\hat{\tau} = \frac{(1, h^{'})}{\sqrt{1 + (h^{'})^2}}$$

$$\hat{n} = \frac{(-h^{'}, 1)}{\sqrt{1 + (h^{'})^2}}$$

$$\frac{1}{\sqrt{1 + (h^{'})^2}} \approx 1 + (h^{'})^2 + \cdots$$

So the linear term for $\hat{\tau}$ and $\hat{n}$ is

$$\hat{\tau} \approx (1, h^{'}) \quad and \quad \hat{n} \approx (-h^{'}, 1) \tag{5.25}$$

We only keep the linearized terms in the following computations.

$$\begin{aligned} u_{i1,\tau} = \hat{\tau} \cdot u_{i1} &= (1, h^{'}) \cdot (u_{i1}, v_{i1}) && (5.26)\\ &= (1, h^{'}) \cdot (u_{01} + u_{11}, 0 + v_{11}) && (5.27)\\ &= u_{01} + u_{11} + \cdots && (5.28) \end{aligned}$$

$$\begin{aligned} \frac{\partial u_{i1,\tau}}{\partial n} &= \hat{n} \cdot \nabla u_{i1,\tau} && (5.29)\\ &= (-h^{'}, 1) \cdot (\frac{\partial u_{i1,\tau}}{\partial x}, \frac{\partial u_{i1,\tau}}{\partial y}) && (5.30)\\ &= (-h^{'}, 1) \cdot (0, u_{01}^{'} + u_{11}^{'}) && (5.31)\\ &= u_{01}^{'} + u_{11}^{'} && (5.32) \end{aligned}$$

Thus,

$$\frac{\partial u_{i1,\tau}}{\partial n}(h) = u_{01}^{'}(h_0) + u_{11}^{'}(h_0) + h_1 u_{01}^{''} + \cdots \tag{5.33}$$

Similarly,

$$\frac{\partial u_{i2,\tau}}{\partial n}(h) = u_{02}^{'}(h_0) + u_{12}^{'}(h_0) + h_1 u_{02}^{''} + \cdots \tag{5.34}$$

Thus we get equation (5.24) since $\mu_1 \frac{\partial u_{01}}{\partial n} = \mu_2 \frac{\partial u_{02}}{\partial n}$ at $h = h_0$.

4. Balance of normal stress:

$$\begin{aligned} \mu_2 \frac{\partial u_{i2,n}}{\partial n}(h) - \mu_1 \frac{\partial u_{i1,n}}{\partial n}(h) &= (p_{i2} - p_{i1}) + \sigma\kappa && (5.35)\\ \Longrightarrow \mu_2 v_{12}^{'}(h_0) - \mu_1 v_{11}^{'}(h_0) &= (p_{12} - p_{11}) - \sigma k^2 h_1(h_0) && (5.36) \end{aligned}$$

Derivation:

$$\kappa = \frac{h_{xx}}{(1+h_x^2)^{3/2}} \tag{5.37}$$
$$= h_{xx}(1+\cdots) \tag{5.38}$$
$$= -k^2 h_{1j} e^{\sigma t + ikx} \tag{5.39}$$

$$u_{i1,n} = \hat{n} \cdot u_{i1} = (-h^{'}, 1) \cdot (u_{i1}, v_{i1}) \tag{5.40}$$
$$= (-h^{'}, 1) \cdot (u_{01} + u_{11}, 0 + v_{11}) \tag{5.41}$$
$$= -h^{'} u_{01} + v_{11} \tag{5.42}$$

$$\frac{\partial u_{i1,n}}{\partial n} = \hat{n} \cdot \nabla u_{i1,n} \tag{5.43}$$
$$= (-h^{'}, 1) \cdot (\frac{\partial u_{i1,n}}{\partial x}, \frac{\partial u_{i1,n}}{\partial y}) \tag{5.44}$$
$$= (-h^{'}, 1) \cdot (0, -h^{''} u_{01} - h^{'} u_{01}^{'} + v_{11}^{'}) \tag{5.45}$$
$$= -h_1^{''} u_{01} - y_1^{'} u_{01}^{'} + v_{11}^{'} \tag{5.46}$$

Similarly, we get

$$\frac{\partial u_{i2,n}}{\partial n} = -h_1^{''} u_{02} - y_1^{'} u_{02}^{'} + v_{12}^{'} \tag{5.47}$$

Plug (5.46) and (5.47) into (5.35) get (5.36).

5. Kinematic free surface condition:

$$h_t = v_1(h) - h_x u(h) \tag{5.48}$$
$$\Longrightarrow \sigma h_1 = v(h_0) - ikh_1 u_0(h_0) \tag{5.49}$$

6. Continuity equation in domain:

$$iku_{i1} + v_{i1} = 0 \tag{5.50}$$
$$iku_{i2} + v_{i2} = 0 \tag{5.51}$$

Stream function

To simplify the system, we introduce a stream function $\psi(x, y, t)$ such that the two components of the disturbance velocity are given by

$$u_1 = \partial\psi/\partial y \qquad \text{and} \qquad v_1 = -\partial\psi/\partial x$$

If we next let

$$\psi(x, y, t) = \phi(y)e^{ikx+\sigma t}$$

then

$$u_1 = \phi^{'} \quad and \quad v_1 = -ik\phi \tag{5.52}$$

disregarding the exponential part. Thus the continuity equation (5.17) is automatically satisfied, and equation (5.18) and (5.19) become:

$$-iku_0^{'}\phi + (\sigma\rho + iku_o - k^2\mu)\phi^{'} - \mu\phi^{'''} = -ikp_1 \tag{5.53}$$

$$-(ik\sigma\rho + ik^3\mu)\phi - iku_0\phi^{'} + ik\mu\phi^{''} = -p_1^{'} \tag{5.54}$$

Solve p_1 from (5.53), then substitute into (5.54), we obtain a fourth-order Orr-Sommerfeld equation:

$$(u_0^{''} + ik\sigma\rho + ik^3\mu)\phi + (iku_0 - u_0^{'})\phi^{'} + (i\sigma\rho k^{-1} - u_0 - 2\mu k)\phi^{''} - ik^{-1}\mu\phi^{''''} = 0 \tag{5.55}$$

Next we formulate the boundary and interface conditions in terms of ϕ.

1. No-slip condition:

$$\phi_1(0) = \phi_1^{'}(0) = 0 \tag{5.56}$$

$$\phi_2(0) = \phi_2^{'}(0) = 0 \tag{5.57}$$

2. Continuity of velocity:

$$\phi_{11}(h_0) = \phi_{12}(h_0) \tag{5.58}$$

$$\phi_{11}^{'} + h_1\phi_{01}^{''}(h_0) = \phi_{12}^{'} + h_1\phi_{02}^{''}(h_0) \tag{5.59}$$

3. Continuity of shear stress:

$$\mu_1(\phi_{11}''(h_0) + h_1\phi_{01}'''(h_0)) = \mu_2(\phi_{12}''(h_0) + h_1\phi_{02}'''(h_0)) \tag{5.60}$$

4. Balance of normal stress: Equation (5.53) gives

$$p_1 = u_o'\phi + (i(\sigma\rho - k\mu) - u_o)\phi' - ik^{-1}\mu\phi'' \tag{5.61}$$

Substitute into equation (5.36), get

$$u_o'(\phi_{12}-\phi_{11})+(i\sigma\rho-u_0)\phi_{12}'(h_0)-(i\sigma\rho-u_0)\phi_{11}'(h_0)-i\mu_2k^{-1}\phi_{12}''+i\mu_1k^{-1}\phi_{11}'-\sigma k^2h_1(h_0) = 0 \tag{5.62}$$

5. Kinematic free surface condition:

$$\sigma h_1 = -ik\phi_1(h_0) - ikh_1u_0(h_0) \tag{5.63}$$

Now we are ready to solve the eigenvalue problem (5.55) numerically subject to boundary and interface conditions $(1-5)$ above. First we discretize ϕ on domain. Let Φ denote the discrete values. The discretized values incorporating boundary and interface conditions can then be written as:

$$A\begin{pmatrix} \Phi \\ h_1 \end{pmatrix} = \sigma B\begin{pmatrix} \Phi \\ h_1 \end{pmatrix}$$

A and B are matrixes. This is a generalized eigenvalue problem which can be solved numerically. σ is the eigenvalues of A. We will like to know if any $Re(\sigma) > 0$ for any wave numbers k.

For the circular arc flow, the system is similar to the system above but with much more complexity since it is two dimensional. However, we should also be able to formulate the corresponding eigenvalue problem numerically. A real difficulty is how to handle perturbations to the contact line. Moving contact line conditions are very poorly understood in literatures.

Chapter 6
Conclusions and Future Work

The unidirectional steady flow of a rivulet driven by gravity and surface tension has been investigated both analytically and numerically. Analytical expressions for the cross-section, fluid velocity and flux have been obtained. The approximate solution gives good agreement with the numerics for contact angles up to 30^o.

The rivulet energy has also been considered to determine whether it is energetically favorable for rivulet break-up. It is found that gravity driven rivulets are unstable to breakup by this mechanism for lengths of the order of millimeters for a range of contact angles but that shear driven rivulets are stable in this way.

An interesting point is that the relation between fluid flux and rivulet width is independent of surface tension in the high surface tension/narrow rivulet scenario. However, surface tension does appear in the low surface tension/wide rivulet result. This surprising result carries through to the non-zero inter-facial shear results.

The asymptotic study of rivulet flow down an inclined surface highlights a strong dependence on the liquid-solid contact angle shown in the flux and energy vs. length plots. This discrepancy may well arise from inaccurate measurements of the contact angle as indicated in [1]. Another source of error is that the analytical results are strictly only valid for a small contact angle, hence a non-negligible correction error is introduced for larger contact angles.

The combined air and rivulet steady flow down a circular channel (ignore gravity) is studied using the annulus model and circular arc model. For the annulus rivulet, the change in pressure

gradient is proportional to the square root of the variation of water flux, for small water fluxes and fixed air flux. Similar result holds for the circular arc rivulet model, but only numerical results are presented due to algebraic complexity of the problem.

For the circular arc model, we also investigated the inverse problem, and found that pressure drop is more sensitive to change channel size than to change in contact angle which relates to the material used to build the channel.

Finally, linear stability of the models are considered. We found from literature that the annulus rivulet is unstable to both asymmetric and axisymmetric disturbances for long wave numbers. Although linear stability analysis based on small perturbation theory predicts instability, more work should be done to investigate the stability problem more thoroughly.

The stability of our circular arc rivulet flow has never been investigated before. One has to study the stability of the circular arc rivulet model numerically. Instead of studing the stability of the circular arc rivulet directly, I present the linearized small perturbation equations and interface/boundary conditions for a simpler rectangular geometry. The immediate next step will be to discretize the domain, resulting in an eigenvalue problem for the growth rates.

More work can be done to improve the asymptotic analysis of rivulet down an inclined plane. We could include the second order term (ϵ^2 terms) in the analysis, and expect that there would be better agreements of the flux and energy vs. length plots between numerics and asymptotics.

In the end, the combined air/water flow model could be tested against experimental data to show its validity.

Appendix

.1 Verification of femlab computation using a rectangular domain

For a rectangular geometry shown below, we have Direchelet conditions on both the top and botom, and Neuman boundary conditions on the two sides. There are also continuity of velocity and stress at the interface. Let $\mu_1 = 1$ in region 1 and $\mu_2 = 2$ in region 2. After applying basic

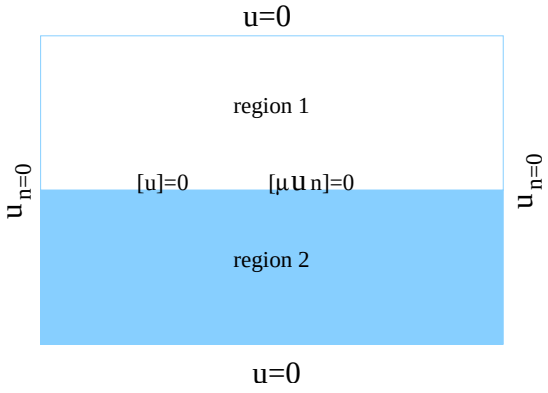

Figure 1: Verification geometry.

techniques, We calculate the exact solution to the PDE. i.e.

$$u = \begin{cases} -\frac{1}{4}y^2 + \frac{7}{24}y \\ -\frac{1}{2}y^2 + \frac{7}{12}y - \frac{1}{12} \end{cases}$$

Integrate over the domain, we find that the flux is 0.05729. Then we used the PDE toolbox in FEMLAB to solve the same problem numerically. And the flux we get is 0.05134 using 100 contour values. Thus the relative error is less than 0.1% . See figure 2 below for the solutions.

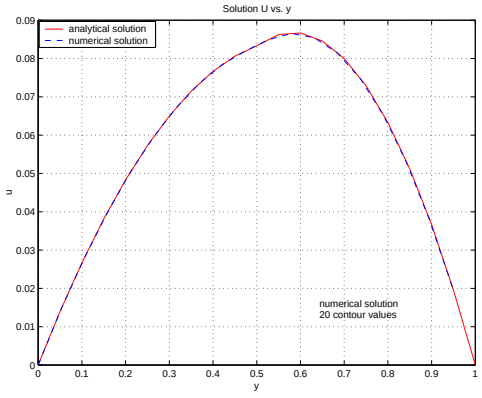

Figure 2: Analytical and numerical solutions

Bibliography

[1] T.G.Myers *Thin films with high surface tension*, Siam Review,40(3), 441-462, 1998.

[2] T.G.Myers, M.H.X.Liang and B.Wetton, *The stability and flow of a rivulet driven by interfacial shear and gravity*, International Journal of Nonlinear-Mechanics, submitted.

[3] Shmuki and Laso, *On the stability of rivulet flow* JFM 215, 125-143, 1990.

[4] Chia-Shun Yih, *Wave formation o a liquid layer for de-icing airplane wings*JFM 212, 41-53, 1990.

[5] T.G.Myers and C.P.Thompson, *Modelling the flow of water on aircraft*, AIAA Journal 36(6) 1010-1013, 1998.

[6] G.K. Batchelor, *An introduction to fluid dynamics*, Cambridge University press.

[7] P.G.Drazin, W.H.Reid *Hydrodynamic stability*, Cambridge University press, 1981.

[8] C.E.Hickox *Instability due to viscosity and density stratification in axisymmetric pipe flow*, Physics of Fluids, **14**(2), 251-262, 1971.

[9] D.Joseph, Y.Renardy *Fundamentals of Two-Fluid Dynamics*, Interdisciplinary Applied Mathematics, Volume **4**, Springer-Verlag.

[10] *Handbook of physics and chemistry*

[11] MATLAB/FEMLAB, The Mathworks Inc., *http://www.mathworks.com.*

[12] E.B.Dussan V, *On the spreading of liquids on solid surfaces: static and dynamic contact lines*, Annual Review of Fluid Mechanics, **11**, 371-400, 1979.

[13] A.C.Fowler *Mathematical models in the applied sciences*, Cambridge texts in applied mathematics, 1997.